12-2014

Cloud Impacts on Pavement Temperature and Shortwave Radiation

Curtis L. Walker
University of Nebraska-Lincoln, curtis.walker@huskers.unl.edu

CLOUD IMPACTS ON PAVEMENT TEMPERATURE AND SHORTWAVE RADIATION

by

Curtis L. Walker

A THESIS

Presented to the Faculty of

The Graduate College at the University of Nebraska

In Partial Fulfillment of Requirements

For the Degree of Master of Science

Major: Earth and Atmospheric Sciences

Under the Supervision of Professor Mark R. Anderson

Lincoln, Nebraska

December, 2014

CLOUD IMPACTS ON PAVEMENT TEMPERATURE AND SHORTWAVE RADIATION

Curtis L. Walker, M.S.

University of Nebraska, 2014

Adviser: Mark R. Anderson

Forecast systems provide decision support for end-users ranging from the solar energy industry to municipalities concerned with road safety. Pavement temperature is an important variable when considering vehicle response to various weather conditions. A complex, yet direct relationship exists between tire and pavement temperatures. Literature has shown that as tire temperature increases, friction decreases which affects vehicle performance. Many forecast systems suffer from inaccurate radiation forecasts resulting in part from the inability to model different types of clouds and their influence on radiation. This research focuses on forecast improvement by determining how cloud type impacts pavement temperature and the amount of shortwave radiation reaching the surface. A preliminary simple radiative transfer model sensitivity study was conducted to determine the relative magnitude of cloud radiative forcing. The study region is the Great Plains where surface radiation data were obtained from the High Plains Regional Climate Center's Automated Weather Data Network stations. Pavement temperature data were obtained from the Meteorological Assimilation Data Ingest System. Cloud type identification was possible via the Naval Research Laboratory Cloud Classification algorithm and clouds were subsequently sorted into five distinct groups; clear conditions, low clouds, middle clouds, high clouds and cumuliform clouds. Distribution and correlation analyses during the daytime in June 2011 revealed that the median pavement temperatures for clear conditions are 40.9 °C, followed by cumuliform clouds at 34.9 °C,

low clouds at 31.5 °C, high clouds at 27.9 °C and the coolest group is middle clouds at 23.7 °C. Similarly, distribution analyses identified maximum median observed surface radiation for clear conditions is 919.0 Wm^{-2}, followed by cumuliform clouds at 800.0 Wm^{-2}, low clouds at 750.0 Wm^{-2}, high clouds at 675.1 Wm^{-2} and the least amount of radiation is associated with middle clouds at 388.4 Wm^{-2}. These pavement temperatures and surface radiation observations were strongly correlated with a maximum correlation coefficient of 0.83. A comparison between cloud-type group identified and cloud cover observed from satellite images provided a measure of confidence in the results and identified cautions with using satellite-based cloud detection. These relationships will be used to develop future model sensitivity analyses to assimilate cloud information directly into pavement temperature energy balance models.

ACKNOWLEDGMENTS

I would like to thank my advisor, Dr. Mark Anderson for his initial hospitality and warm welcome during my recruitment visit, and his continued support of my research activities throughout my program of study. Further, I would also like to thank Dr. Clinton Rowe and Dr. Jun Wang for agreeing to serve on my thesis committee in addition to their feedback both in and out of the classroom.

I would like to thank my colleagues Thomas Polivka and Xiaoguang Xu for their assistance with programming and working with radiative transfer models and various satellite data sets.

I thank all of my fellow graduate students, faculty and staff within the Department of Earth and Atmospheric Sciences for their support, time, friendship, consideration and resources.

I thank my former and current collaborators at the National Center for Atmospheric Research in Boulder, Colorado whom I met during my time in the Significant Opportunities in Atmospheric Research and Science (SOARS) Program. I especially must express my gratitude towards Mr. Michael Chapman, Ms. Amanda Anderson and Dr. Sheldon Drobot for their contributions to data acquisition and processing suggestions.

One cannot forget family and loved ones, so I thank my close family scattered across the country and newly formed family for their support through the development of this thesis and long-distance phone calls.

GRANT INFORMATION

This material is based upon work supported by the American Meteorological Society Graduate Fellowship (2012-2013) sponsored by ITT Exelis.

This material is based upon work supported by the National Science Foundation Graduate Research Fellowship under Grant No. DGE-1041000. Any opinion, findings, and conclusions or recommendations expressed in this material are those of the author and do not necessarily reflect the views of the National Science Foundation.

TABLE OF CONTENTS

1. INTRODUCTION

Weather forecasts are produced to serve a variety of applications which affect the decisions of various end-users. One such application is pavement temperature forecasting. Pavement temperature forecasts provide critical information to local officials, transportation industry interests and the general public whether traveling for business or pleasure. These forecasts can help guide decisions such as when to treat roads during snowstorms and when the weather will be ideal for maintenance projects. Pavement temperature information can lead to recommendations for shipping companies to avoid potentially troublesome routes which can save time and money evading hazardous conditions, lowering lengthy and costly detours. Forecast accuracy is crucial for these end-users as slight variations can cost substantial time and resources.

These forecasts must account for tremendous situational variability. Meteorological conditions such as presence or lack of precipitation, season and air mass can induce forecast errors. Topography and elevation introduce further complexity. Site specific information such as whether or not a particular road segment is composed of concrete or asphalt, or lies on a bridge deck make forecasting more challenging, yet pavement temperature forecasts perform fairly well despite such challenges (Crevier and Delage 2001). The use of pavement temperature information is becoming more widespread with technological advancements (NCAR 2014a) and emphasis on weather risk assessment and decision support initiatives (e.g., Weather-Ready Nation, NOAA 2014). As the use of pavement temperature forecasts becomes more widespread, one recurring source of forecast error is the influence of cloud cover. Clouds act to damp the

diurnal variation of pavement temperatures and existing models often have difficulty parameterizing such localized effects of cloud cover (Drobot et al. 2012).

Pavement temperature forecasting during cloud cover has been mentioned as an issue (Bogren 1991), however, no attempts have been made to consider an independent cloud observation data set with spatiotemporal resolution that would be sufficient for the purposes of a forecasting application. Current strategies to resolve this cloud problem in pavement temperature models are for any conditions other than completely clear, to assume that the model is 100% cloudy (Drobot et al. 2012). Such a correction, while not perfect, still does better than a clear sky pavement temperature forecast. Still, greater refinement is needed and there is a gap in the literature concerning issues of pavement temperature forecasts and subsequent decision making.

This research proposes a unique approach to the challenge of pavement temperature forecasting during cloud cover by developing a method to spatiotemporally compare satellite-based cloud information with surface pavement temperatures. Further, quantifying how clouds influence pavement temperatures through their effect on atmospheric radiative transfer will be explicitly considered in the analyses. Statistical analyses reveal important relationships among observed pavement temperature, surface radiation and cloud cover data. The analyses also show limitations in available cloud data. Understanding the relationships, correlations and limitations among cloud cover and observed pavement temperatures are paramount to forecast improvement. The results of these analyses will serve as a foundation for eventual assimilation of these relationships and satellite-based cloud information directly into pavement temperature models.

2. BACKGROUND

There is an increasing amount of recent literature recognizing the necessity for improved forecasting of the impacts of hazardous weather events and decision support for local officials concerning the nation's surface transportation corridors. The literature currently provides an excellent account of the present hazards and future avenues for improvement; however, little addresses the challenges sought after by this research. There is little known literature presently bridging the issues of pavement temperature forecasting and the influence of cloud cover.

a. Road Weather Hazards

Weather-related vehicular crashes are defined by the United States Department of Transportation (USDOT) Federal Highway Administration (FHWA) Road Weather Management Program (FHWA 2014) as those crashes that occur in adverse weather conditions (i.e., rain, sleet, snow, and/or fog) or on slick pavement (i.e., wet pavement, snowy/slushy pavement, or icy pavement). Twenty-four (24) percent of all crashes in the United States are weather-related and these crashes account for an annual average of 7,130 fatalities and over 629,000 injuries each year (Pisano et al. 2008). When considering that the average cost per crash according to the National Highway Traffic Safety Administration in 2000 was $14,100 and that 20% of state department of transportation budgets are devoted to snow and ice control operations, these weather-related crashes and mitigation strategies account for billions of dollars each year in congestion delays to shipping companies as well as property damages, medical bills and liability suits (Pisano et al. 2008).

The key factors that lead up to the occurrence of a weather-related crash are conditions that either impedes vehicle performance (i.e., the pavement condition) or driver ability (i.e., weather condition). In terms of vehicle performance, Chen et al. (2009) considered the effects of physics, topography and weather on the likely occurrence of a crash. Their work identified an "accident speed limit" threshold given a certain set of conditions present. Overall, their analysis identified that rapid decelerations were among the most dangerous maneuvers that motorists could engage in during poor weather conditions. In terms of mitigation strategies, the ability to forecast pavement temperatures across desired road segments remains a crucial piece of information in reducing the risks associated with hazardous weather conditions. Khasawneh and Liang (2012) demonstrated an inverse relationship between the coefficient of friction for hot-mix asphalt and pavement temperature. Higher pavement temperatures were associated with reduced friction and grip between the road surface and a vehicle's tires. Their study considered only dry pavement as the frictional effects of precipitation tend to be larger in magnitude and previously discussed in the literature (e.g., Pisano et al. 2008), yet little research has considered the dry situation.

Pavement temperature forecasting is growing in importance among forecasters and others concerned with offering decision support to local officials. Rutz and Gibson (2013) recently provided a first-time perspective from the National Weather Service (NWS) of incorporating pavement temperature forecasts and associated model results into decision support applications. The current model of choice for pavement temperature forecasting is Environment Canada's Model of the Environment and Temperature of Roads (METRo; Crevier and Delage 2001). This model has the ability to forecast both

the pavement temperature as well as the condition of the road surface based on initial conditions from both Road Weather Information System (RWIS) station data and the Canadian Meteorological Centre's (CMC) Global Environmental Multiscale (GEM) model. It is important to note that METRo can be coupled with any numerical weather prediction model (e.g., Weather Research and Forecasting model). METRo is composed of three modules that assess: 1) the energy balance module for the road surface, 2) a heat-conduction module for the road material, and 3) a module to handle water, snow, and ice accumulation on the roadway. The key inputs for this model are; incoming radiation flux, road surface albedo, latent heat flux, water vapor flux, temperature, humidity, wind speed, road specific heat capacity and thermal conductivity, and precipitation accumulation on the road. At this time, a limitation of the model is its inability to assess the influence of passing vehicles and maintenance operations on roadway conditions (i.e., precipitation accumulation). METRo has the ability to operate in an automated mode which initializes the model and runs based on RWIS data and GEM output, or a manual mode in which radiation fluxes are interpolated and parameterized from cloud cover forecasts. A unique feature of the model is its ability to make adjustments to negate the effect of microclimates by creating short-term forecasts and reassessing the performance of these forecasts to tune itself for a given region, during its coupling phase between initialization and forecasting. A 2007 study conducted by the National Center for Atmospheric Research (NCAR) found that the METRo generally outperformed similar pavement temperature forecasting models (NCAR 2014b). A later NCAR study (Drobot et al. 2012) critiques the generally poor performance of METRo and similar models under variably cloudy conditions. Their consensus was that surface

energy balance models such as METRo were not accurate with respect to the radiative transfer influence of clouds due to numerous parameterizations and approximations that are used in such models. The primary METRo parameterization for cloud cover considers the cloud area fraction (i.e., observed station octets of cloud cover) which provides a sense of overall cloud cover but not the type of cloud that is influencing the radiative transfer and surface energy balance relationships.

b. Clouds, Instantaneous Radiative Flux, Surface Energy Balance and Cloud Detection

The METRo operates as a surface energy balance model and must accurately consider atmospheric radiative transfer relationships. Current literature tends to focus on the role of clouds in the entire climate system (e.g., Stephens 2005). The research presented in this paper is focused on the radiative properties of clouds on short time periods and small spatial scales. Clouds influence radiative transfer in both the shortwave and longwave radiation spectrum. Downwelling shortwave radiation (i.e., radiation from the sun to the surface) is important to this study because it is necessary for pavement temperature modeling. Further, it is better to begin by quantifying shortwave radiation and later refining the methods to include the complexities of longwave radiation.

Stephens and Tsay (1990) are among the first to call attention to prior miscalculations of cloud radiative properties. They note discrepancies between theoretical and observed values for cloud absorption and reflection. Their results highlight the importance of two cloud parameters: extinction coefficient and single-scatter albedo. Both parameters describe the transparency of a medium to shortwave radiation transmission. The larger these parameters, the more opaque the medium is to shortwave

radiation. These parameters will be important for later studies and eventual cloud identification techniques. The general theory outlines a complex relationship between droplet size and cloud absorption as a function of both absorption strength and optical thickness (liquid water path).

As previous work shows, various cloud parameters affect the magnitude of cloud influence to radiative transfer. Varnai and Davies (1999) provide a theoretical framework for how individual photons traverse a cloud layer. Their work may be interpolated to transmission of solar radiation through a particular cloud. A better understanding of how such physical properties of clouds (e.g., shape, depth) affect shortwave radiation has been integral to the development of algorithms capable of identifying various cloud types.

The work of Chen et al. (2000) lays the foundation for the development of modern cloud identification algorithms. They specifically assess the diverse radiative effects of different cloud types. In their study, clouds are categorized according to their optical thickness and cloud top height. A simple radiative model is used to simulate a particular cloud type's radiative influence at the top of the atmosphere (TOA) and near the surface. They are careful to note that their findings are for broad, global areas. The effect of a particular cloud type on a localized scale cannot be explicitly determined from these results. The current research will focus on localized cloud radiative influences.

Radiative transfer models are capable of ingesting various cloud parameters as inputs and use known radiative transfer relationships to predict expected radiative flux at various levels in the atmosphere. One such radiative transfer model used in this analysis is the Santa Barbara Discrete Ordinates (DISORT) Atmospheric Radiative Transfer

Model (SBDART; Ricchiazzi et al. 1998). The SBDART model computes plane-parallel radiative transfer quantities for a variety of situations. The model has adopted six standard atmospheric profiles to simulate prototypical conditions in the following climate regimes; tropical, midlatitude summer, midlatitude winter, subarctic summer, subarctic winter, and US62 which represents typical conditions over the continental United States. Also the model contains five basic surface covers to simulate ocean water, lake water, vegetation, snow and sand. The user can create hybrid combinations of these surface conditions to simulate more realistic environments. Radiative transfer quantities for cloud atmospheres are computed with a Mie scattering code which parameterizes extinction efficiency, single scattering albedo, and asymmetry factor as a function of optical thickness. Known molecular and aerosol radiative influences are also included in the SBDART model. Subsequent analyses in this paper will capitalize on the SBDART model's ability to simulate radiative transfer with respect to clouds and water vapor.

Radiative transfer models provide a simulated approach to understanding how radiation interacts with atmospheric constituents. Real observations provide a ground truth to compare and improve such models. These observations are often obtained from satellite-based platforms. One such endeavor was the National Aeronautics and Space Administration's (NASA) Clouds and Earth's Radiant Energy System (CERES) experiment (Wielicki et al. 1996). CERES data sets rely on information obtained from both geostationary and polar-orbiting satellites. These satellites are capable of computing expected radiative fluxes in addition to real-time ground observations. The superiority of these observing platforms and relationship to the current research is that they also provide

observations of cloud and aerosol radiative transfer properties such as optical thickness and single scatter albedo that can be cross-examined with ground-based observations.

Real-time observations of such cloud properties yield the opportunity to identify and classify clouds based on those same properties. Several studies have developed, evaluated and improved cloud classification algorithms. Ackerman et al. (2008) assess the performance of the Moderate Resolution Imaging Spectroradiometer (MODIS) cloud mask algorithm. Their discussion is pertinent to the present research since radiometer data will be incorporated into the comparison. The MODIS algorithm classifies regions as cloudy if the optical depth exceeds 0.4; this limitation is significant, particularly for high, thin cloud scenarios. Liu et al. (2011) utilize the whole-sky infrared cloud-measuring system (WSIRCMS) to develop a classification scheme based on the structural appearance of clouds in the infrared range. This algorithm is capable of identifying cirriform clouds based on wispy and feathery appearance, waveform clouds by the recurrence of clouds in a mass or roll-like pattern, cumuliform clouds based on a cotton ball appearance and stratiform clouds due to their blanket-like shape. In Ackerman et al. (2008), cirriform clouds present a challenge for the MODIS algorithm due to their small optical depth. Yang et al. (2012) developed an automated cirrus cloud detection algorithm for ground-based cloud identification. This algorithm utilizes a background subtraction adaptive threshold (BSAT) method. The significance of this research is two-fold: the algorithm is able to detect cirrus clouds accurately and it is able to do so from the surface. Satellite technology is expensive and the refinement of relatively inexpensive ground-based detection will be an advantage going forward. Further, satellite cloud detection only provides description of the cloud “canopy” and fails to provide an

accurate assessment of complex cloud situations with multiple levels of assorted cloud types. Ground-based cloud detection, despite its benefits, would only accurately identify the lowest cloud layers and is limited in its spatiotemporal availability, and was not considered for the current research objectives.

The Naval Research Laboratory (NRL) Cloud Classification (NRLCC) algorithm for the operational National Oceanic and Atmospheric Administration's Geostationary Observational Environmental Satellites (NOAA – GOES) (Bankert 1994; Tag et al. 2000; Bankert and Wade 2007; Bankert et al. 2009) is a supervised classifier, unlike algorithms which are unsupervised and automated. Supervised classification means that the algorithms have been "trained" to identify clouds with a data set that was manually classified by experts. Clouds are classified on a pixel-by-pixel basis utilizing a 1-nearest neighbor method (1 NN) by a combination of visible (daytime only) and infrared satellite imagery as soon as they are available. Despite a brief gap between daytime and nighttime classifications due to channel switching, this particular cloud classifier is capable of both day and night operation to provide quasi-continuous cloud information. The explicit physics of the algorithm categorizes general cloud types (e.g., clear, partly cloudy, liquid water, supercooled water, mixed phase, etc.). The implicit physics is capable of describing specific cloud type subdivisions (e.g., cirrus, cirrocumulus, cirrostratus, etc.). This near-real time, post-processing algorithm was selected for the current analysis. The goal of this research is to develop a method for spatiotemporally matching NRLCC algorithm output with pavement temperature and surface radiation observations to develop a quantitative understanding of the influence of clouds. Such results may be used in future research to directly improve pavement temperature forecasts.

3. METHODS

This research analysis seeks to quantify the influence of clouds on short-term variability on pavement temperature and to consider such variability in downwelling shortwave radiation, hereafter referred to as "surface radiation". This research represents the first known instance of pairing surface pavement temperature observations with remotely sensed satellite cloud detection from the NRLCC algorithm. Pavement temperature, surface radiation, and cloud types were obtained during the month of June 2011 primarily due to data availability; this time period allowed for relatively uniform TOA solar radiation (i.e., consider solar analemma) and there was spatiotemporal data consistency. Daytime hours are the primary daily time period of interest given the research objective of understanding the role of clouds in influencing surface radiation and pavement temperatures. It is important to first understand daytime shortwave radiation because it allows for the development of methods that can then be applied to the additional complexities presented by consideration of longwave radiation in future assessments. Further, the literature has shown that cloud cover most influences daytime pavement temperatures.

a. Study Region and Data

This study required a region that both occupied the satellite domain and contained a comprehensive meteorological surface data network for both surface radiation data and pavement temperatures. For these reasons, the study region for this work was defined by the political boundaries of North Dakota, Nebraska, Kansas and Iowa (Figure 3.1).

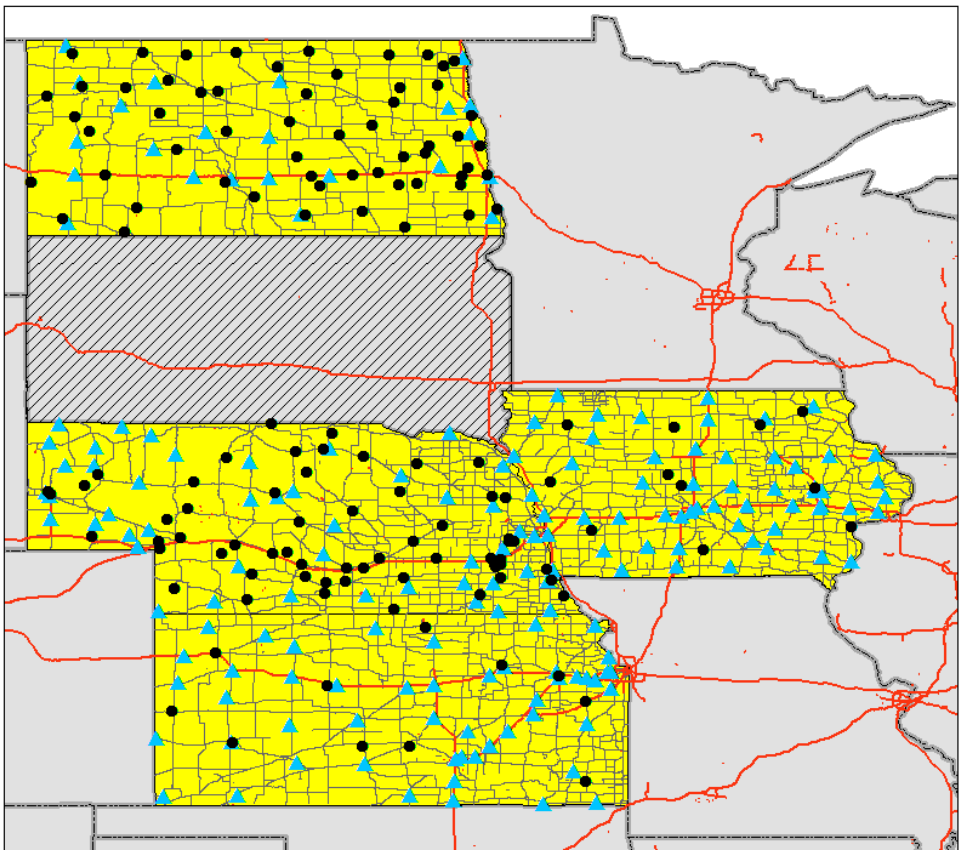

Figure 3.1. Study region; yellow states were those whose observations and data are used in the analyses. High Plains Regional Climate Center's Automated Weather Data Network (AWDN) stations (black dots) provide high quality surface radiation observations. Meteorological Assimilation and Data Ingest System (MADIS) Road Weather Information System (RWIS) stations (blue triangles) provide pavement temperature data throughout the study region with primary and secondary roadways also marked within the study states. South Dakota is hatched because it was removed due to data inconsistency.

Surface radiation data (Changnon et al. 1990) were obtained from the High Plains Regional Climate Center's Automated Weather Data Network (AWDN; HPRCC 2013). This network provides observation points spread throughout the Great Plains (Figure 3.1). Surface radiation data from each site were obtained hourly. It is important to note that such temporal resolution does not allow an assessment of instantaneous cloud influences, though broad statistical assessment and distribution analyses are possible.

Surface pavement temperature data were obtained via the National Oceanic and Atmospheric Administration's Meteorological Assimilation Data Ingest System (MADIS 2014) archived at the NCAR High Performance Storage System (HPSS; NCAR 2014c). Due to a lack of reporting pavement temperature data to MADIS, South Dakota was not included in the study region (Figure 3.1). MADIS pavement temperature data are measured from RWIS stations throughout the study region with a temporal resolution of approximately every ten minutes. There are approximately 175 RWIS stations included in this analysis. These observations were obtained from a variety of RWIS configurations (i.e., flat road surfaces, bridge decks, overpasses, underpasses, etc.). There are two primary types of sensors from which pavement temperature observations are obtained. In-pavement sensors, such as the FP 2000 (Vaisala 2014), resemble a hockey puck and lie within the road surface, approximately two centimeters below the surface providing more of an in-situ pavement temperature. Infrared sensors, such as the DST111 (Vaisala 2014) sit perched adjacent to the road surface approximately 9.1 meters (30 feet) above the ground, providing more of a skin pavement temperature. State departments of transportations do not provide consistent nor extensive metadata for their respective RWIS networks, therefore, controlling for the site configuration and sensor type was not

performed in this analysis. Further, the research objective is to quantify the influence of clouds cover on pavement temperature in a broad context, so such control was deemed not necessary.

Cloud type detection output from the NRLCC algorithm (NRL 2013) was also obtained from the NCAR HPSS. The NRLCC algorithm post-processes GOES satellite imagery. The temporal resolution of NRLCC algorithm is every 15 minutes. The combination of visible and infrared satellite channels from GOES imagery allows for 4 km spatial resolution. These data were matched spatiotemporally with RWIS station observations. The NRLCC algorithm output provides 25 unique satellite-based cloud and surface cover classifications (Table 3.1). Only the daytime cloud type classifications were later grouped into categories for this analysis.

b. Preliminary Analysis – Simple Radiative Transfer Model

The first step in the analysis involved a simplified radiative transfer model sensitivity study using the output from the SBDART model (SBDART 2013). The goal of the sensitivity study was to demonstrate the relative importance of clouds and their associated properties on surface radiation compared to that of water vapor. In this study, downwelling spectral irradiance is considered at the TOA and at the surface. The typical solar spectrum is considered with an initial wavelength (WLINF) of 0.25 μm to a final wavelength (WLSUP) of 1.0 μm. The wavelength increment (WLINC) used was 0.005 μm. Downwelling spectral irradiance (BOTDN) was converted to total irradiance for each of the sensitivity tests by the following equation:

Table 3.1. NRLCC algorithm categories (Bankert and Wade 2007).

NRLCC Algorithm Categories	Description
1	Stratus (St)
2	Stratocumulus (Sc)
3	Cumulus (Cu)
4	Altocumulus (Ac)
5	Altostratus (As)
6	Cirrus (Ci)
7	Cirrocumulus (Cc)
8	Cirrostratus (Cs)
9	Cumulus Congestus (CuC)
10	Cs associated with deep convection
11	Cumulonimbus (Cb)
12	Clear (ground or ocean)
13	Snow covered ground
14	Haze (smoke, dust, etc.)
15	Sun glint
16	Low clouds (Night)
17	Midlevel clouds (Night)
18	High, thin clouds (Night)
19	High, thick clouds (Night)
20	Cumulus congestus (Night)
21	Deep convection (Night)
22	Thin, high over low clouds (Night)
23	Open-celled cumulus (Night)
24	Snow-covered ground (Night)
25	Clear (ground or ocean, Night)

$$F = 0.005 * \Sigma (BOTDN_{(i)}) \quad (1)$$

Where F is total irradiance in Wm^{-2}, $BOTDN_{(i)}$ is the downwelling spectral irradiance measured at each wavelength. Total irradiance computed from the SBDART model is analogous to surface radiation.

For modeling the radiative influence of clouds, key parameters that are computed for each layer include the extinction efficiency, single scattering albedo and the asymmetry factor. In terms of the SBDART model, the cloud parameter inputs that were modified to test the sensitivity of surface radiation included cloud optical thickness (TCLOUD), cloud altitude (ZCLOUD), and the effective radius of cloud particles (NRE). Cloud types were defined from Hartmann et al. (1992) and Ricchiazzi et al. 1998 based on the TCLOUD and ZCLOUD parameters. The radiative influence of each cloud type and the differences in influence between cloud types are considered. Table 3.2 summarizes the input parameters and descriptions for the cloud model sensitivity analysis. These parameter choices were supported by the previous literature (e.g., Hartmann et al. 1992, Richiazzi et al. 1998) as the albedo of 0.30 represents a general Earth albedo and the tropical atmosphere is representative of a typical air mass for the study region in the month of June. Further, Crevier and Delage (2001) define pavement albedo between 0.1 and 0.5 for the METRo.

For modeling the radiative influence of water vapor, there are a few ways in which SBDART accounts for water vapor variability. In this study, an SBDART parameter (IDATM) that assumes standard values of atmospheric composition for five "typical" atmospheres is used. From each of these atmospheres, variable water vapor concentration values are considered as well as their influence on downwelling spectral

Table 3.2. SBDART input parameters for cloud radiometric property sensitivity runs (Hartmann et al. 1992, Ricchiazzi et al. 1998).

SBDART Environment Parameters		**Input Value**	**Description**
IDATM		1	Tropical Atmosphere
ISALB		0	Uniform Surface Albedo
ALBCON		0.3	Surface Albedo
SZA		30	Solar Zenith Angle
SBDART Cloud Parameters			
Cloud-Type Group	**SBDART Input**		
Low	TCLOUD	16, 1	Cloud Optical Thickness (bottom, top)
	ZCLOUD	1, -3	Cloud Layer Height (1-3 km)
	NRE	10, 20; 80, 90	Effective Radii (10-20; 80-90 μm)
Thin-Middle	TCLOUD	2, 1	Cloud Optical Thickness (bottom, top)
	ZCLOUD	4, -6	Cloud Layer Height (4-6 km)
	NRE	10, 20; 80, 90	Effective Radii (10-20; 80-90 μm)
Thick-Middle	TCLOUD	32, 1	Cloud Optical Thickness (bottom, top)
	ZCLOUD	4, -8	Cloud Layer Height (4-8 km)
	NRE	10, 20; 80, 90	Effective Radii (10-20; 80-90 μm)
Thin-High	TCLOUD	2, 1	Cloud Optical Thickness (bottom, top)
	ZCLOUD	7, -9	Cloud Layer Height (7-9 km)
	NRE	10, 20; 80, 90; -10, -20	Effective Radii (10-20; 80-90 μm; 10-20 μm ice)
Thick-High	TCLOUD	32, 1	Cloud Optical Thickness (bottom, top)
	ZCLOUD	7, -11	Cloud Layer Height (7-11 km)
	NRE	10, 20; 80, 90; -10, -20	Effective Radii (10-20; 80-90 μm; 10-20 μm ice)

irradiance and total irradiance. All other parameters in these atmospheres were held constant to only detect the water vapor signal. Table 3.3 summarizes the input parameters and descriptions for the water vapor model sensitivity analysis.

c. Analysis of Clouds and Pavement Temperature

The second step in the analysis after determining the relative importance of clouds and water vapor from a theoretical framework is to observe and quantify the role of clouds on influencing surface radiation and subsequent pavement temperatures in an applied setting. It is necessary to isolate and extract the cloud information from the NRLCC algorithm pixel containing and pixels surrounding the pavement temperature sensor. The pixel containing the pavement temperature sensor and the surrounding eight pixels are selected and their cloud type information extracted (Figure 3.2). This nine pixel box (3x3 pixels) provides 12 km resolution of pavement temperature related to cloud-type group. This resolution is acceptable given the spatial distribution of RWIS stations throughout the study region and the fact that cloud-type groups are generally spatially consistent (Hartmann et al. 1992, Chen et al. 2000). Then, for each time stamp, the clouds are grouped into general types based on height characteristics (Table 3.4), and the most frequent of the general cloud types for all nine pixels is assigned to the surface observation for the time stamp. This is termed the "modal cloud." Hereafter these modal cloud assignments will be referred to as cloud-type groups.

For quality control purposes, the following criteria are imposed on individual pavement temperature sites on a state-by-state daily basis. At the state level, a mean pavement temperature is computed for the pavement temperature time series along with associated standard deviations for a single day. A site was removed from the data set if

Table 3.3. SBDART input parameters for water vapor radiometric property sensitivity runs (Hartmann et al. 1992, Ricchiazzi et al. 1998).

SBDART IDATM	Precipitable Water Vapor (gcm^{-2})	Atmosphere Description
1	4.117	Tropical
2	2.924	Mid-latitude Summer
3	0.854	Mid-latitude Winter
4	2.085	Sub-arctic Summer
5	0.418	Sub-arctic Winter
6	1.418	US62 Standard

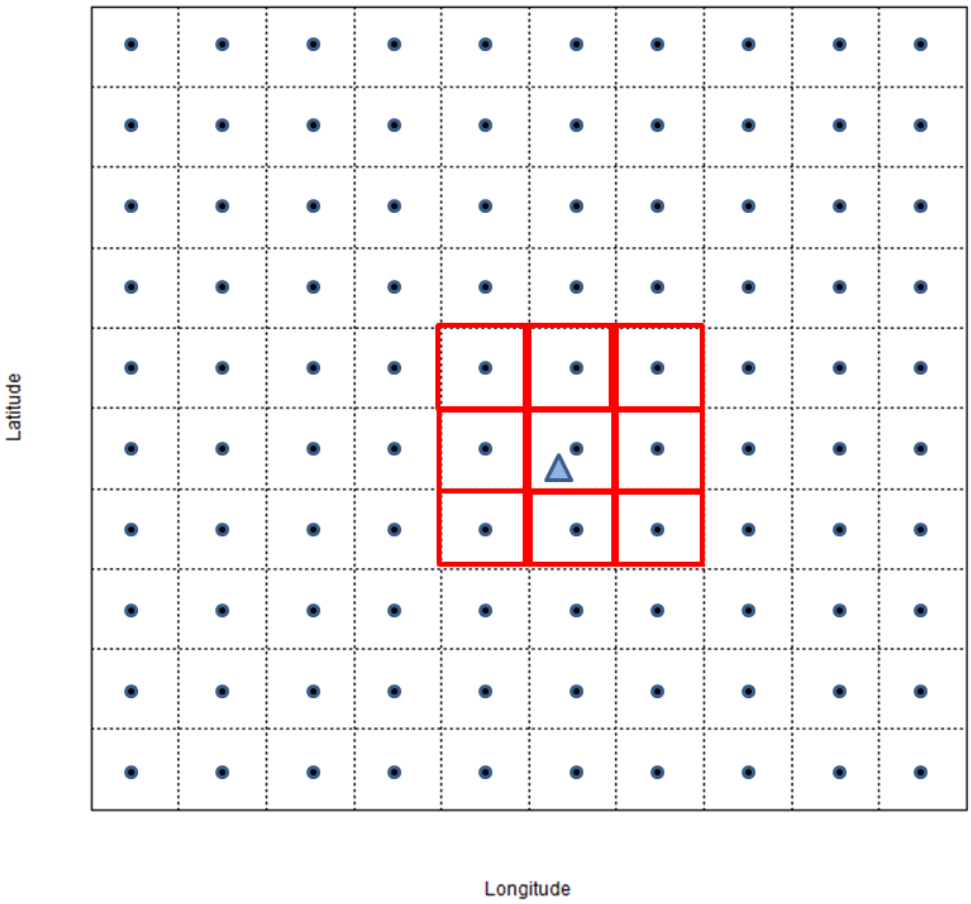

Figure 3.2. Schematic of method to spatially relate pavement temperature sensors (blue triangle) with NRLCC algorithm data. The grid-cell spacing is 4 km resolution and each centroid represents a longitude, latitude coordinate pair from the NRLCC algorithm. The red boxes denote the pixels selected for extracting cloud information which includes the pixel containing the pavement temperature site as well as the surrounding pixels.

Table 3.4. Cloud-type groups arranged by height for the analysis.

Cloud-Type Groups			
Low	***Middle***	***High***	***Cumuliform***
Stratus Stratocumulus	Altocumulus Altostratus	Cirrus Cirrostratus Cirrocumulus	Cumulus Cumulus Congestus Cumulonimbus Cirrostratus Anvil

more than 50% of its observations are greater than two standard deviations from the mean in any of the following three time periods on that particular day: 0000 UTC to 1159 UTC, 1200 UTC to 2359 UTC, or 0000 UTC to 2359 UTC. This process was repeated each day, for all states in order to identify if particular sites experienced a malfunction for a period of time or if something anomalous occurred. Although nocturnal cloud observations are not considered in this analysis, the overnight time period is still used in the quality control criteria to have a more stringent requirement on the entire data set. A "bad" site at night might have some measurement error that would propagate into the daytime as well, though it may be masked by a day with a complex cloud-type group assortment. An example pavement temperature time series (Figure 3.3) contains sites that have been flagged for removal as they exceeded the threshold for a particular period of time. It is important to note that throughout the data set, sites that violated the criteria did so for an extended period of time. There were very few instances in which a site was marginal in terms of adherence to the quality control criteria. There tended to either be a noticeable violation or the site was deemed appropriate to remain in the analysis.

d. Case Study Selection

After matching cloud observations to those of pavement temperatures and considering the data set as a whole, it was desirable to consider a smaller subset of the data for more detailed analyses. Due to inconsistencies in the RWIS data, there were some discontinuities within the data set (Figure 3.4). Four dates were omitted from the June 2011 analysis; 17, 19, 23, and 28 June. On 21 June the Kansas pavement temperature time series shows several discontinuities (Figure 3.5). Further RWIS data availability consideration revealed that no data were available for Kansas after 21 June.

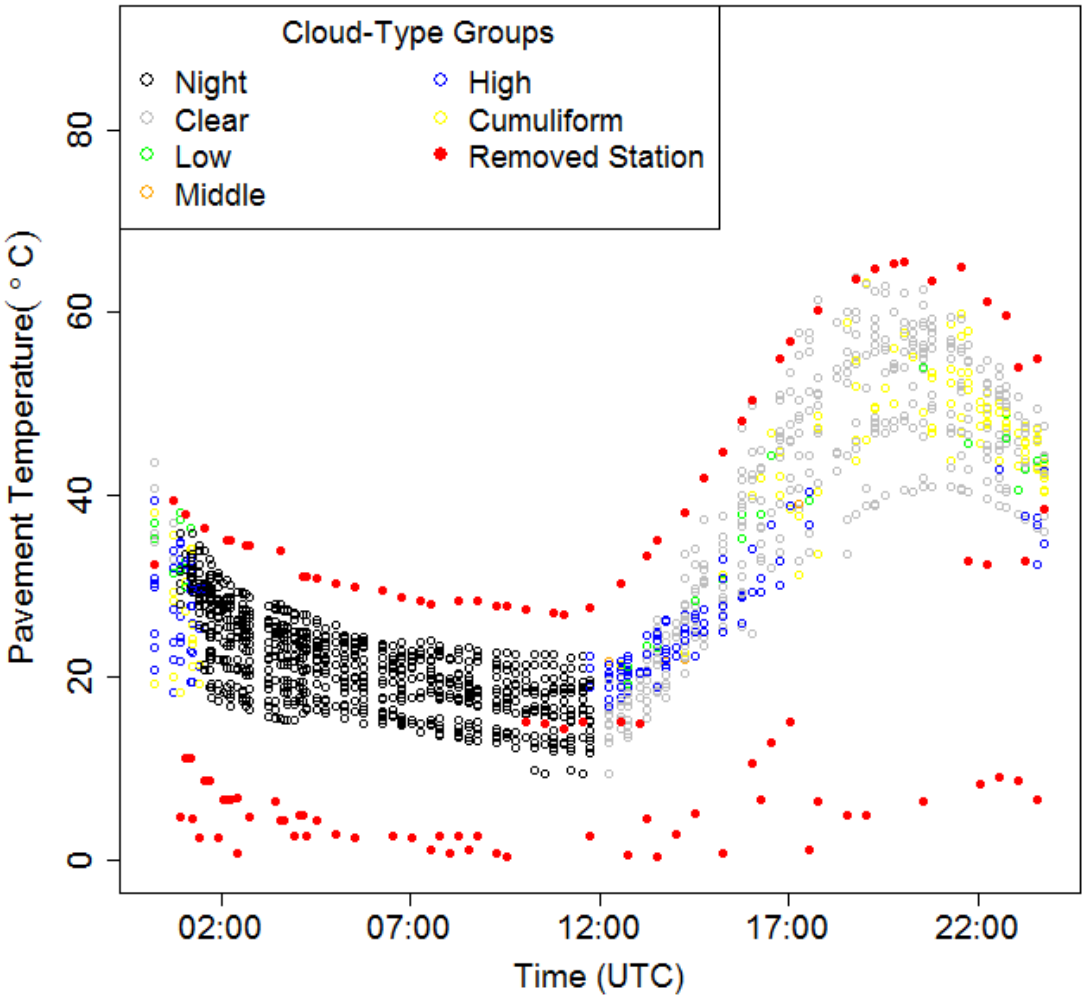

Figure 3.3. Example pavement temperature quality control time series from 12 June 2011 in Nebraska. Observations are color-coded according to cloud-type groups and sites in red have been flagged for removal by the quality control criterion.

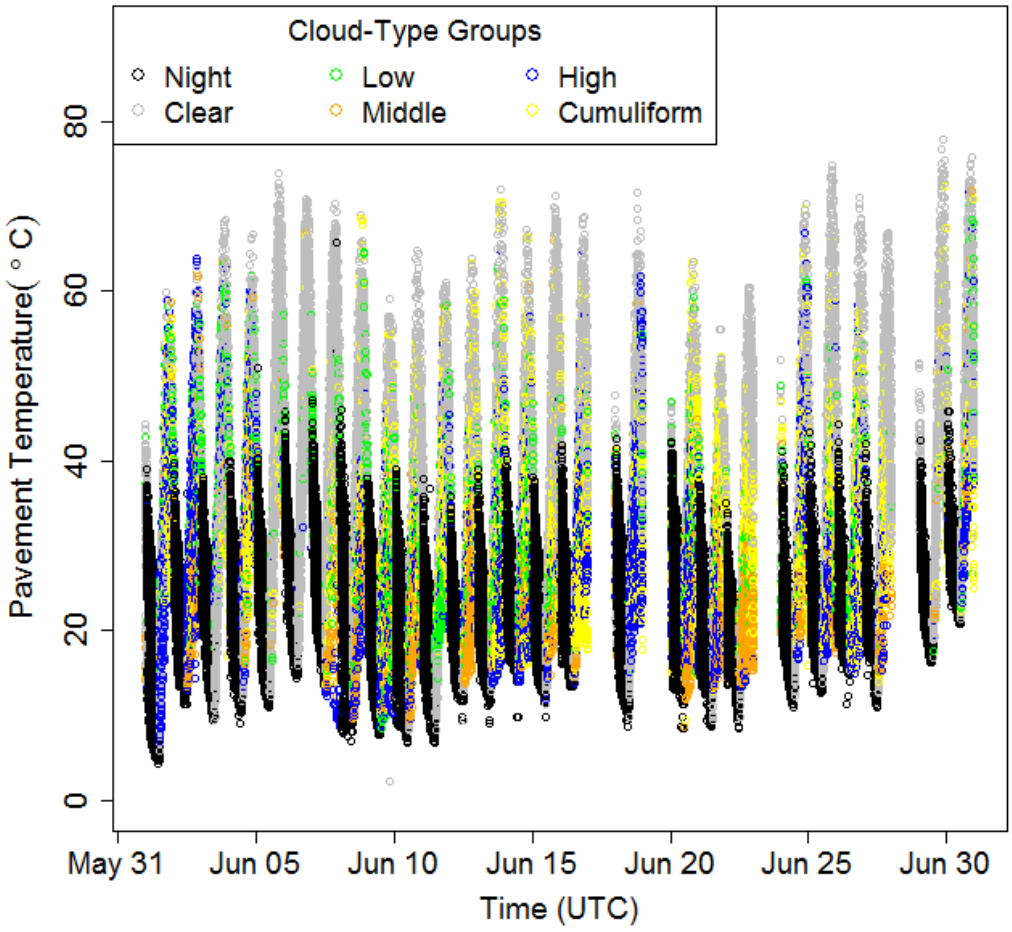

Figure 3.4. June 2011 pavement temperature time series shows missing RWIS data.

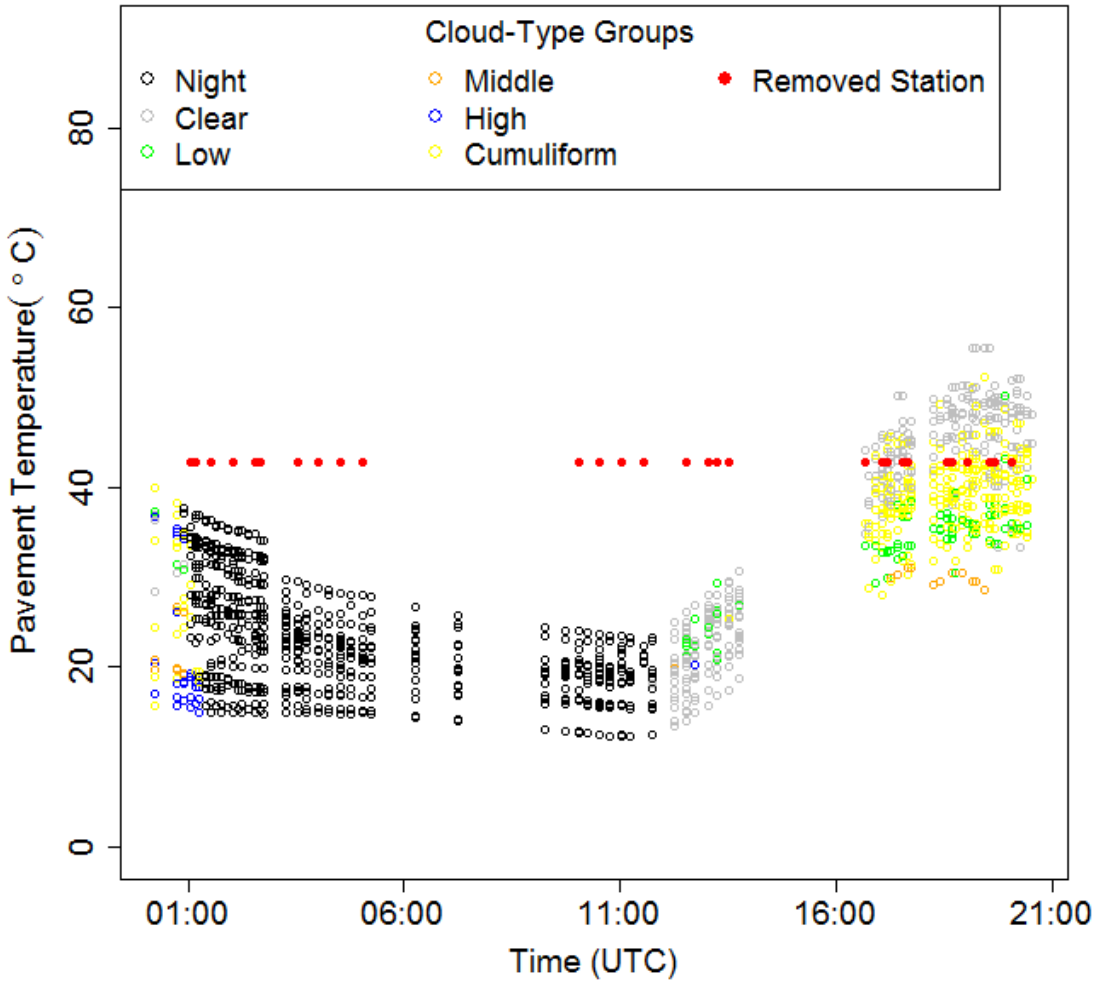

Figure 3.5. Kansas pavement temperature time series on 21 June 2011. Observations are color-coded according to cloud-type groups and sites in red have been flagged for removal by the quality control criterion.

For the purposes of data continuity (Figure 3.6), the period from 1-16 June 2011 was parsed from the June 2011 data set. This allowed for just over two weeks of pavement temperature observations to be compared with the month as a whole to ensure that the subset was representative of the variability among cloud cover and pavement temperature. These 16 days were then classified as either clear or cloudy based on whether or not a simple majority of pavement temperature observations had a modal cloud classification of clear or some type of cloud cover present (Table 3.5). An equal number of days were classified as either clear or cloudy. For later analyses and based on the percentages, 1 June was further sub-defined as a partly cloudy day given the nearly equal number of cloud versus clear observations, 6 June was deemed a representative clear day and 9 June was deemed as a representative cloudy day. While 6 June was the day with the highest number of clear observations, 9 June was the day with the second largest number of cloudy observations. The cloudiest day, 2 June, was not selected as the representative cloudy day as there was a brief data discontinuity overnight (Figure 3.7).

After defining representative case study days and a smaller subset, a method to remove diurnal dependence was defined. The aforementioned June 2011 distribution analysis comparisons do not remove diurnal or daily variability. For example, a particular day could have higher pavement temperatures than another due to synoptic meteorological conditions (e.g., cold front passage). A simpler example is to compare time of day (TOD). Morning sunrise is associated with cooler temperatures than midday peak solar heating. In order for a less biased comparison of the data, observations were rearranged and compared based on TOD. Five key TODs were defined for each day from 1-16 June 2011; sunrise (12 UTC), morning (15 UTC), midday (18 UTC), afternoon

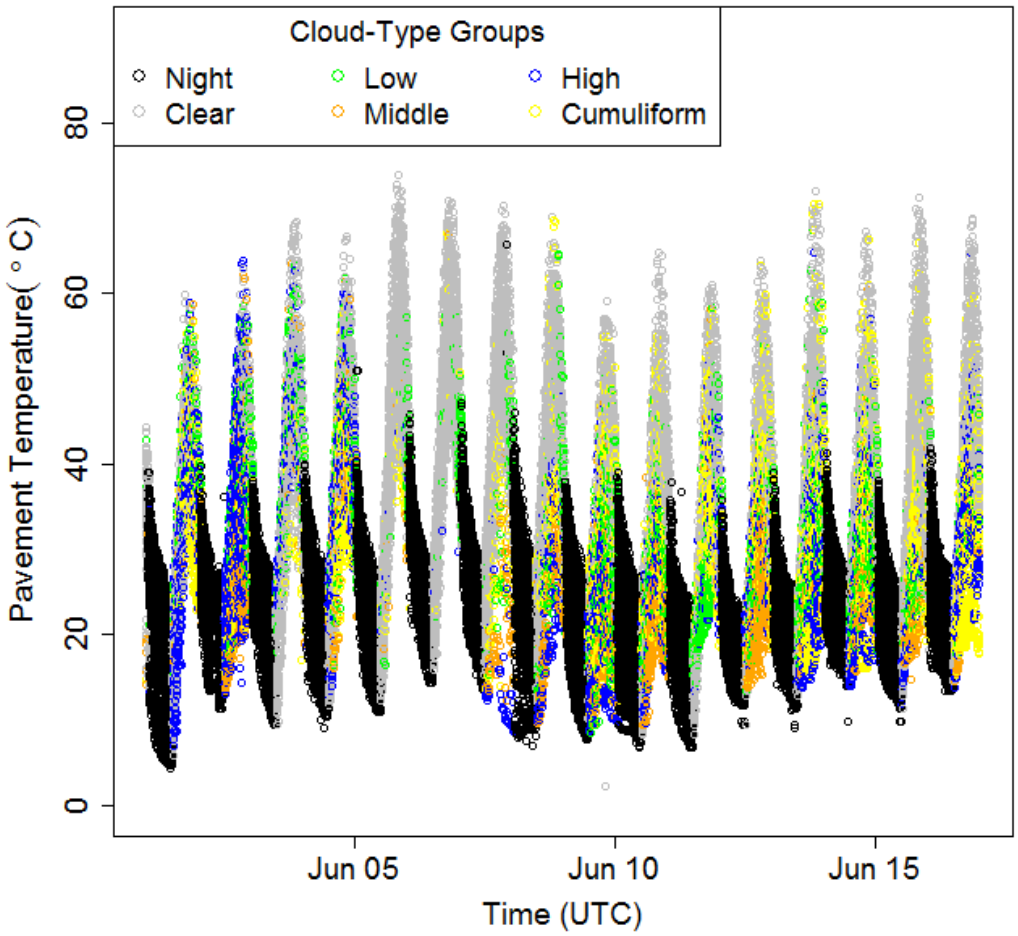

Figure 3.6. Continuous 1-16 June 2011 pavement temperature time series exhibits day-to-day variability in cloud cover and pavement temperature.

Table 3.5. Number of pavement temperature observations 1-16 June 2011 defined as either clear or cloudy and declaration for each day.

Date (June 2011)	Clear Observations (%)	Cloudy Observations (%)	Day Classification
1	2103 (51.0)	2024 (49.0)	CLEAR
2	558 (13.2)	3680 (86.8)	CLOUDY
3	2368 (58.3)	1691 (41.7)	CLEAR
4	1820 (27.4)	4821 (72.6)	CLOUDY
5	3194 (84.1)	605 (15.9)	CLEAR
6	4212 (93.5)	295 (6.5)	CLEAR
7	5140 (89.8)	585 (10.2)	CLEAR
8	4910 (73.4)	1779 (26.6)	CLEAR
9	1242 (21.2)	4631 (78.8)	CLOUDY
10	1000 (24.0)	3167 (76.0)	CLOUDY
11	1571 (38.8)	2476 (61.2)	CLOUDY
12	1280 (30.9)	2864 (69.1)	CLOUDY
13	1530 (39.4)	2351 (60.6)	CLOUDY
14	1227 (31.1)	2718 (68.9)	CLOUDY
15	2551 (67.4)	1233 (32.6)	CLEAR
16	2075 (51.6)	1944 (48.4)	CLEAR

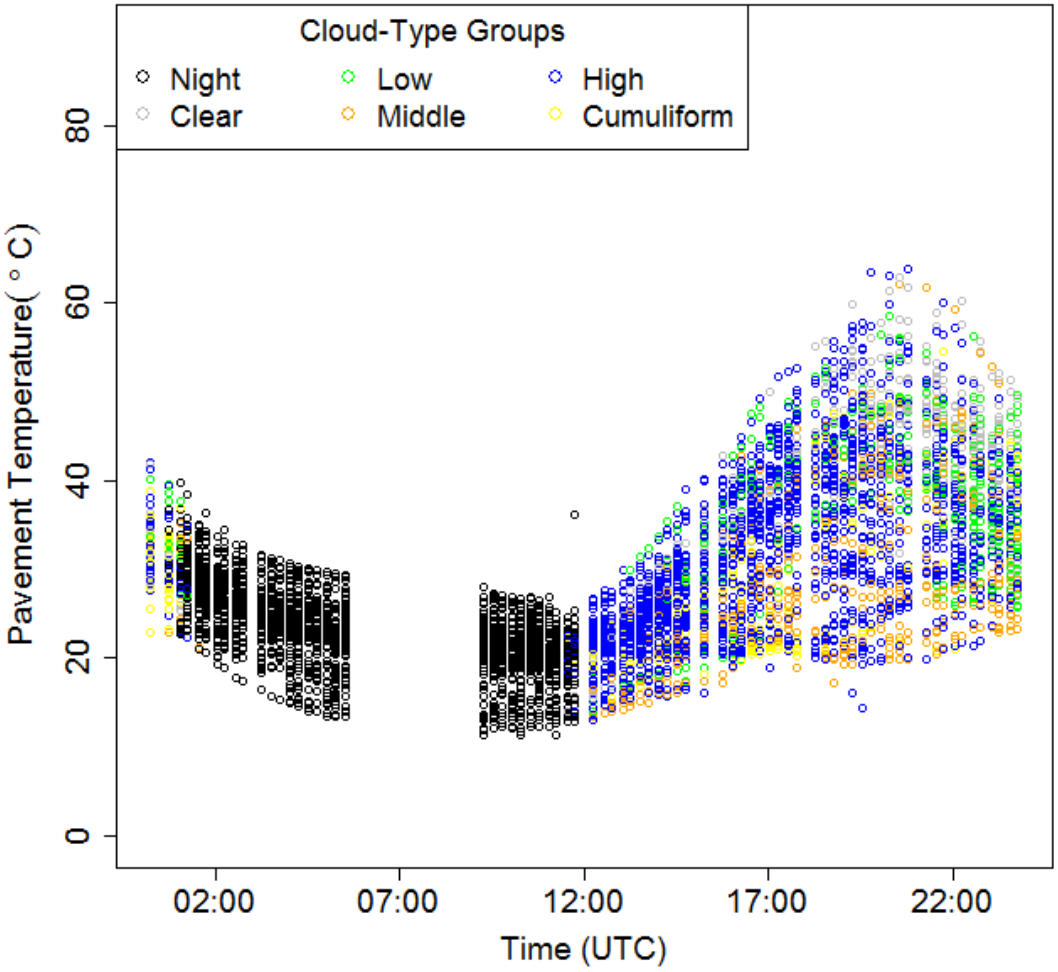

Figure 3.7. Pavement temperature time series on 2 June 2011 exhibits an overnight discontinuity whose cause and effect remain unknown.

(21 UTC) and sunset (00 UTC). These time periods were not selected arbitrarily but rather defined by whether or not the NRLCC algorithm was in its day mode or night mode. Sunrise and sunset were identified based on the first available time stamp in which all sites throughout the study region did not observe a nighttime cloud observation. It is important to note that this induces about a one hour difference in the amount of sunlight a across the study region. For example, a site in the eastern part of the study region will have had daylight for an hour whereas a site in the western part of the study region would only have sunlight for a few minutes. Three hour increments were then used to establish the remaining three TODs. Typical peak solar heating occurred between midday and afternoon. Time series and distribution analyses for each cloud-type group were analyzed at each TOD. Hourly distributions were also computed in order to compare the pavement temperature distribution throughout the day for each cloud-type group. The value of removing the diurnal trend allows for a less biased comparison of the pavement temperature and cloud-type group observations, but also reveals synoptic trends and station characteristics within the data set (Figure 3.8). On 5 June 2011, the time series shows an anomalously cool site despite overall lack of cloud cover. Closer inspection reveals that this site represents a section of Nebraska Highway 35 near Hubbard, NE (Figure 3.9). This site appears to be associated with a bridge which is a likely explanation for its cooler temperature. Further, the time series hints at the synoptic conditions with a weak sinusoidal tendency observed in the pavement temperature time series. Consideration of the synoptic weather pattern reveals that a cold front progressed through the region on 9 June 2011 which was associated with clear conditions prior to the frontal passage and an increase in cloud cover post-frontal (Figure 3.10).

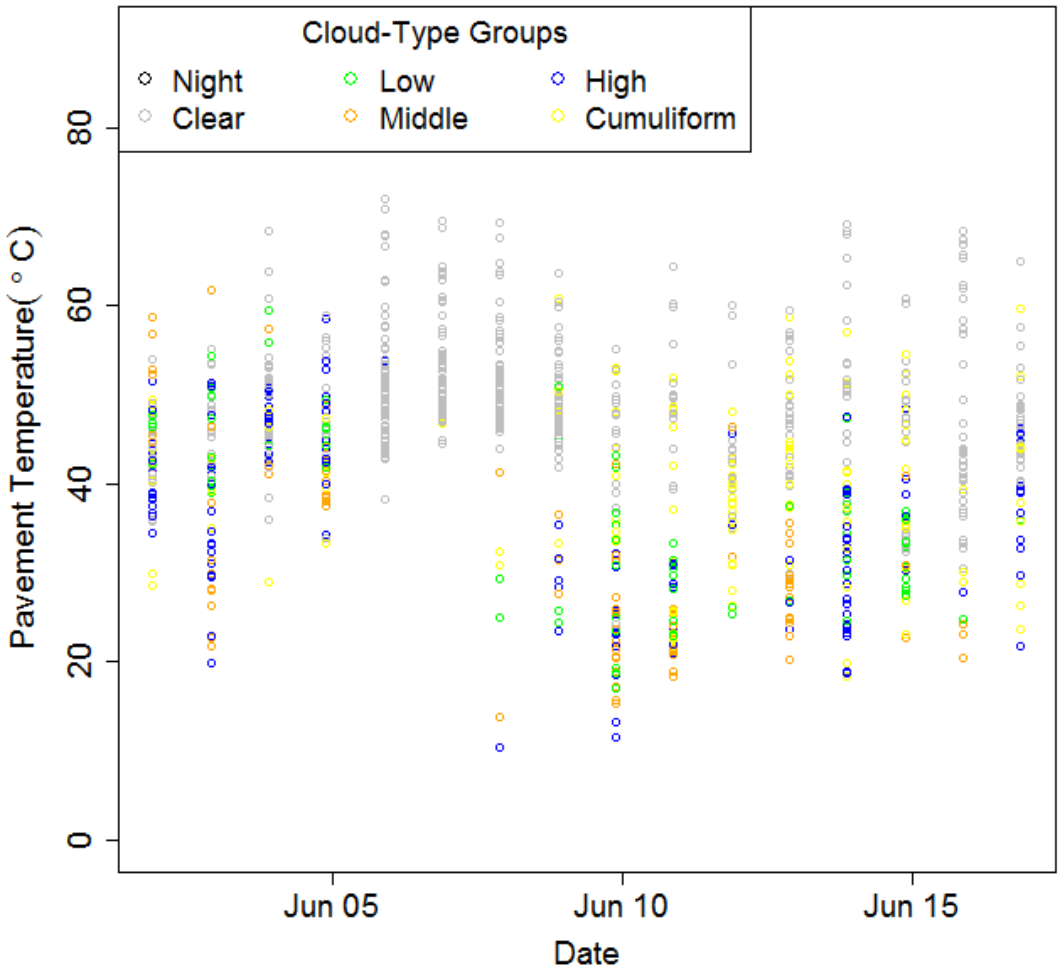

Figure 3.8. Pavement temperature time series from 1-16 June 2011 for all afternoons (21 UTC) removes diurnal dependence and exhibits synoptic meteorological pattern as well as individual site variability.

Figure 3.9. Google Maps image of Highway 35 RWIS site (red circle) near Hubbard, NE over an irrigation extension to Pigeon Creek (Google 2014).

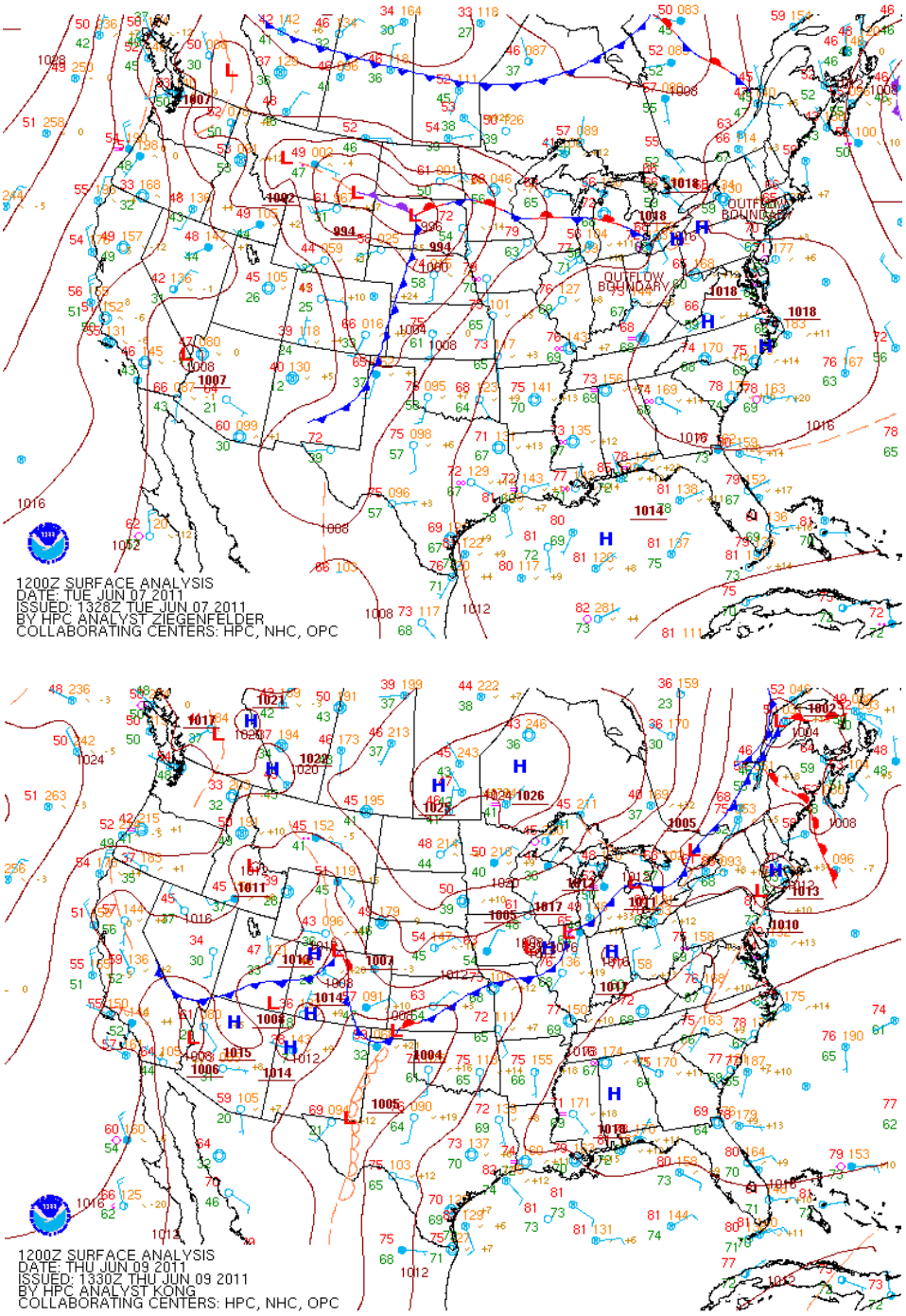

Figure 3.10. Weather Prediction Center archived surface analysis data shows frontal passage between 12 UTC 7 June 2011 (top) and 12 UTC 9 June 2011 (bottom). The pre-frontal environment is associated with higher temperatures, clearer skies and southerly winds. The post-frontal environment is characterized by cooler temperatures, increased cloud cover and winds with a northerly component (WPC 2014).

e. Identification of Correlation Among Clouds, Pavement Temperature and Radiation

Surface radiation observations from AWDN sites were included in the analysis based on the proximity between an RWIS and AWDN sites. A spatial threshold of 12 km was used in order to be consistent with the same spatial resolution of matching RWIS sites with NRLCC algorithm cloud output (Figure 3.2). Seventeen total pairs of matched AWDN and RWIS sites were identified based on the spatial threshold criterion, though data inconsistencies reduced this number to 13 sites (Table 3.6). Similar to the pavement temperature and cloud-type group analyses, distributions of surface radiation among the cloud-type groups was considered only at the specific TODs to remove diurnal and sun angle bias for more meaningful comparisons and discussion.

Correlation and other statistical analyses were performed to measure the relationships among cloud-type groups, pavement temperatures and surface radiation observations. These analyses were performed for the 1-16 June 2011 period on all 13 sites rather than the individual case study days or individual sites due to the relatively small sample size of such comparisons. The statistical analyses were also considered for the entire 1-16 June 2011 data and separately on each TOD. Nighttime observations were omitted from the statistical analyses entirely.

f. Cross-Validation: Cloud Identified Versus Satellite Imagery

Archived visible satellite images were obtained from the NOAA Comprehensive Large-Array Data Stewardship System (CLASS 2014). These images were originally from the operational GOES with a 1 km spatial resolution allowing for high-quality

Table 3.6 Matched (12 km threshold) Automated Weather Data Network (AWDN) and Road Weather Information System (RWIS) sites.

Site Number	AWDN	RWIS
1	Hofflund, ND	Ray, ND US-2 MP 51.3
2	Wishek, ND	Wishek, ND ND-3 MP 40.7
3	Fargo, ND	Fargo, ND I-94 Railroad Bridge
4	Bowman, ND	Bowman, ND US-85 MP12.2
5	Mandan, ND	Bismarck, ND I-94 Bridge
6	Scottsbluff, NE	Highway 71 South of Beltline
7	Halsey, NE	Dunning-Middle Loup Bridge
8	Newport, NE	Newport, NE on Highway 20 at MP 273
9	Cedar Rapids, IA	Cedar Rapids, IA US-30
10	Garden City, KS	US-50 at K-156 Bridge
11	Manhattan, KS	K-177
12	Silverlake, KS	I-470 Bridge over US-75
13	Silverlake, KS	US-75

consideration of various cloud scenarios. These images were later cross-examined with the NRLCC algorithm output. The intent is to provide a preliminary, qualitative feasibility assessment of the output from the NRLCC algorithm. The CLASS archived visible satellite images were spatiotemporally matched with algorithm output for the three case days (1 June, partly cloudy; 6 June, clear; and 9 June, cloudy). The RWIS locations were plotted on the visible satellite image and color coded according to the cloud-type groups identified by the NRLCC algorithm. This cross-examination assessment can also be considered a check on the nearest pixel matching method between NRLCC algorithm output and the RWIS sites.

4. RESULTS AND DISCUSSION

The primary research objective is achieved through the quantification of pavement temperature and cloud-type group distribution analyses. The radiative transfer model sensitivity provides initial insight into the relative magnitude of influence to surface radiation from clouds and water vapor. The subsequent case study analyses allow for better understanding of how cloud cover affects pavement temperature through influencing surface radiation. Though water vapor is important to consider in atmospheric radiative transfer, the sensitivity study shows the relative magnitude of water vapor influence to surface radiation compared to that of cloud cover is negligible.

a. Simple Radiative Transfer Model Sensitivity Study

Hartman et al. (1992) and Chen et al. (2000) have demonstrated several possible methods of developing cloud type classification based on cloud optical thickness and cloud altitude. In this sensitivity analysis, the cloud-type groups and appropriate parameters shown by Hartman et al. 1992 and Ricchiazzi et al. 1998 are used to test surface radiation sensitivity to a series of cloud parameters (Table 3.1). Low clouds are the first to be simulated in the SBDART model. Two distinct effective radii ranges are used to show the radiative differences between low clouds with relatively small cloud particles and those with relatively large cloud particles. The difference can be thought of as comparing a low stratus cloud producing drizzle (small cloud particles) with a low nimbostratus cloud that is producing rain (precipitation particles). Recall that (1) gives us total irradiance which is spectral irradiance integrated over wavelength, in this case the visible spectrum since we are considering shortwave. For low clouds, the two effective

radii ranges do not appear to produce substantial differences in the downwelling spectral irradiance (Figure 4.1). For cloud particles with effective radii in the 10-20 μm range, the surface radiation is 378.0 Wm^{-2}. Surface radiation with cloud particles in the 80-90 μm range is 397.7 Wm^{-2} (Table 4.1). While it is important to not misinterpret the magnitude of this difference, it does highlight the relationship between the size parameter and extinction efficiency. As size increases, extinction efficiency generally decreases slightly. This principle explains why there is a slightly larger total irradiance associated with the larger effective radii range. The larger sized particles allow more direct and diffuse light to pass between them as there are fewer particles overall to impede transverse radiation.

Middle clouds are subdivided into thin and thick categories based on their respective optical thickness values. For each subdivision, the same two effective radii ranges are considered. The first observation is the relative importance of cloud optical thickness compared to effective radius in terms of radiative influence (Figure 4.2). The model surface radiation for thin middle clouds with small cloud particles is 668.2 Wm^{-2} and 674.8 Wm^{-2} for large particles. For thick middle clouds with small and large particles, surface radiation is 251.2 Wm^{-2} and 266.3 Wm^{-2}, respectively (Table 4.1). The difference in surface radiation when considering effective radius is on the order of 10 Wm^{-2}. The difference in irradiance between thin and thick clouds as a function of cloud optical thickness is an order of magnitude larger (400 Wm^{-2}). This result supports the notion that cloud optical thickness is one of the most important cloud properties regarding radiative influence. Effective radius variability seemed to produce a slightly larger irradiance range for thick clouds than thin suggesting a dependence of optical thickness on cloud particle size (Figure 4.2).

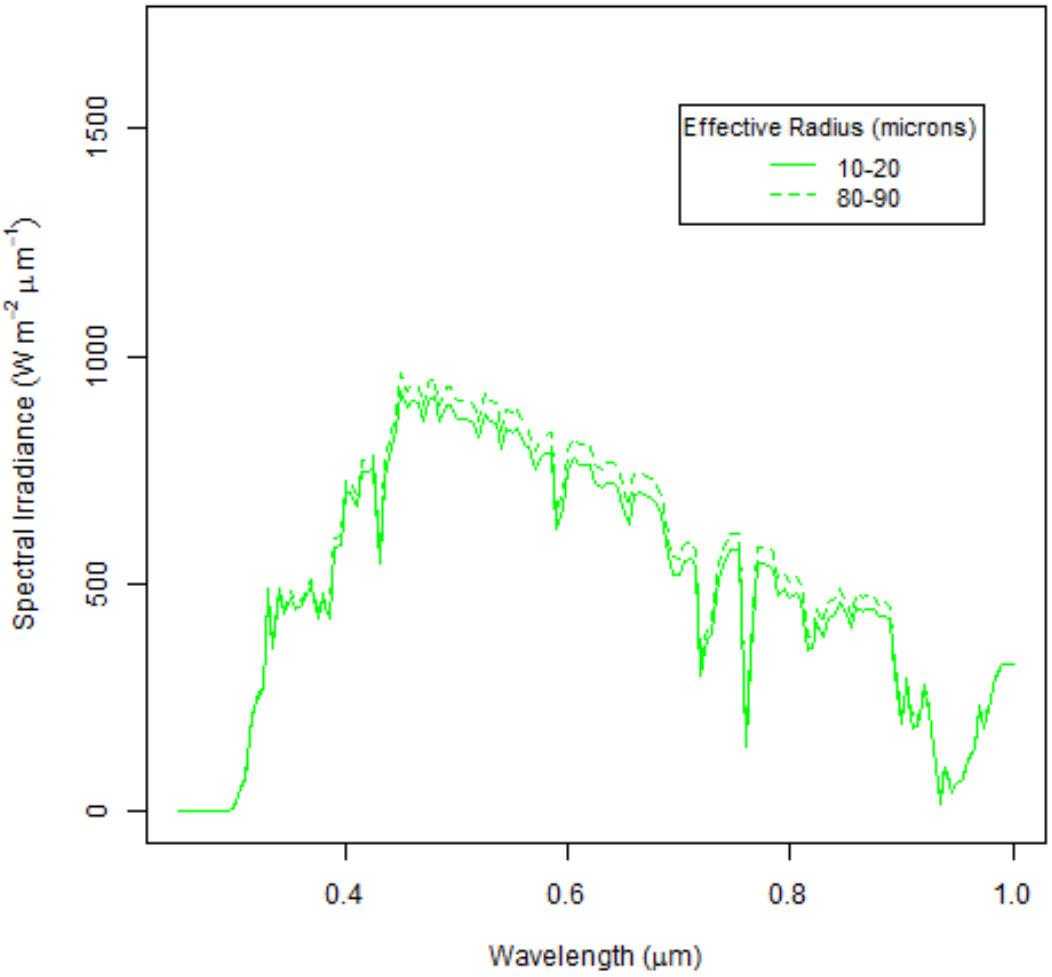

Figure 4.1. Downwelling spectral irradiance at the surface for low clouds with effective radii from 10-20 μm (solid line) and 80-90 μm (dashed line).

Table 4.1. Summary of surface radiation for cloud type sensitivity test runs. Small particle size denotes effective radii from 10-20 μm, large particle size denotes effective radii from 80-90 μm, and ice particle size refers to ice particles with effective radii from 10-20 μm.

Cloud-Type Group	**Particle Size**	**Surface Radiation** (Wm^{-2})
Low	Small	378.0
	Large	397.7
Thin-Middle	Small	668.2
	Large	674.8
Thick-Middle	Small	251.2
	Large	266.3
Thin-High	Small	668.6
	Large	675.3
	Ice	672.7
Thick-High	Small	251.9
	Large	266.9
	Ice	263.9

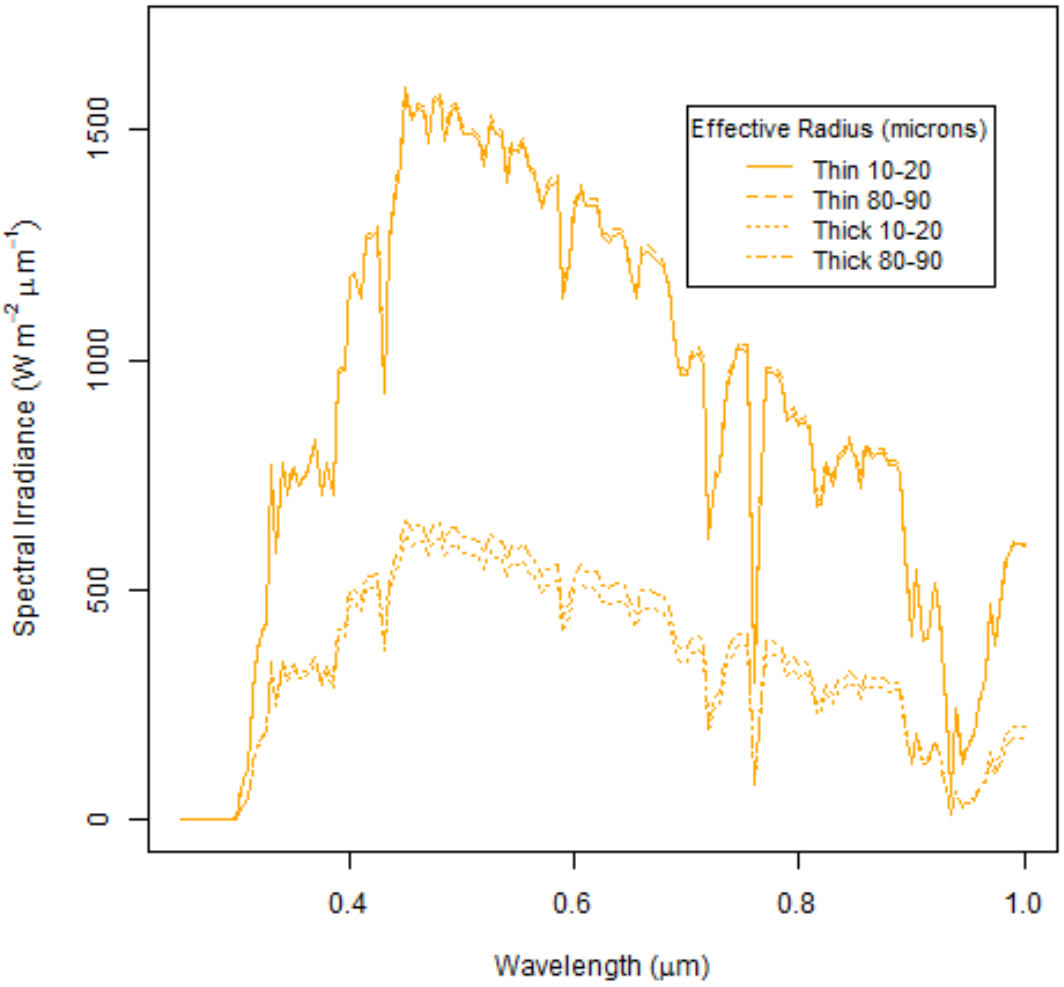

Figure 4.2. Downwelling spectral irradiance at the surface for thin middle and thick middle clouds with effective radii from 10-20 μm and 80-90 μm.

High clouds are further subdivided among thin and thick clouds with small cloud particles, large cloud particles and ice cloud particles (Figure 4.3). Similar trends are observed as with middle clouds. In particular, the variability between thin and thick is substantially more pronounced than radiation variability associated with effective radius (Table 4.1). Irradiance values associated with ice phase particles tended to fall between small and large cloud particles. Also similar to middle clouds, there is a larger range of irradiance values associated with thicker clouds rather than their thin counterparts.

The most important observation from these cloud sensitivity runs is the importance of cloud optical thickness in governing the variability in irradiance (Figure 4.4 and Table 4.2). Notice that, at least for the visible spectrum, there are similar irradiance values for thin middle/high clouds and for thick middle/high clouds. This indicates that cloud height had a relatively small role in governing radiative properties. Clouds with similar optical thicknesses will have a similar effect on the surface radiation. As for low clouds, their radiative impact may also be somewhat masked by the input parameters that define them (Table 3.2). Low clouds (366.9 Wm^{-2}) would likely be similar to their middle/high counterparts if only a similar cloud optical thickness value was used.

The final sensitivity run considered the influence of variations in water vapor concentration on surface radiation. Various water vapor concentrations are simulated based on typical global atmospheres packaged with SBDART. The relative influence of variations in atmospheric water vapor concentration does not produce substantial differences in surface downwelling spectral irradiance (Figure 4.5). As water vapor concentration increases, surface radiation decreases slightly (Table 4.3). Simply

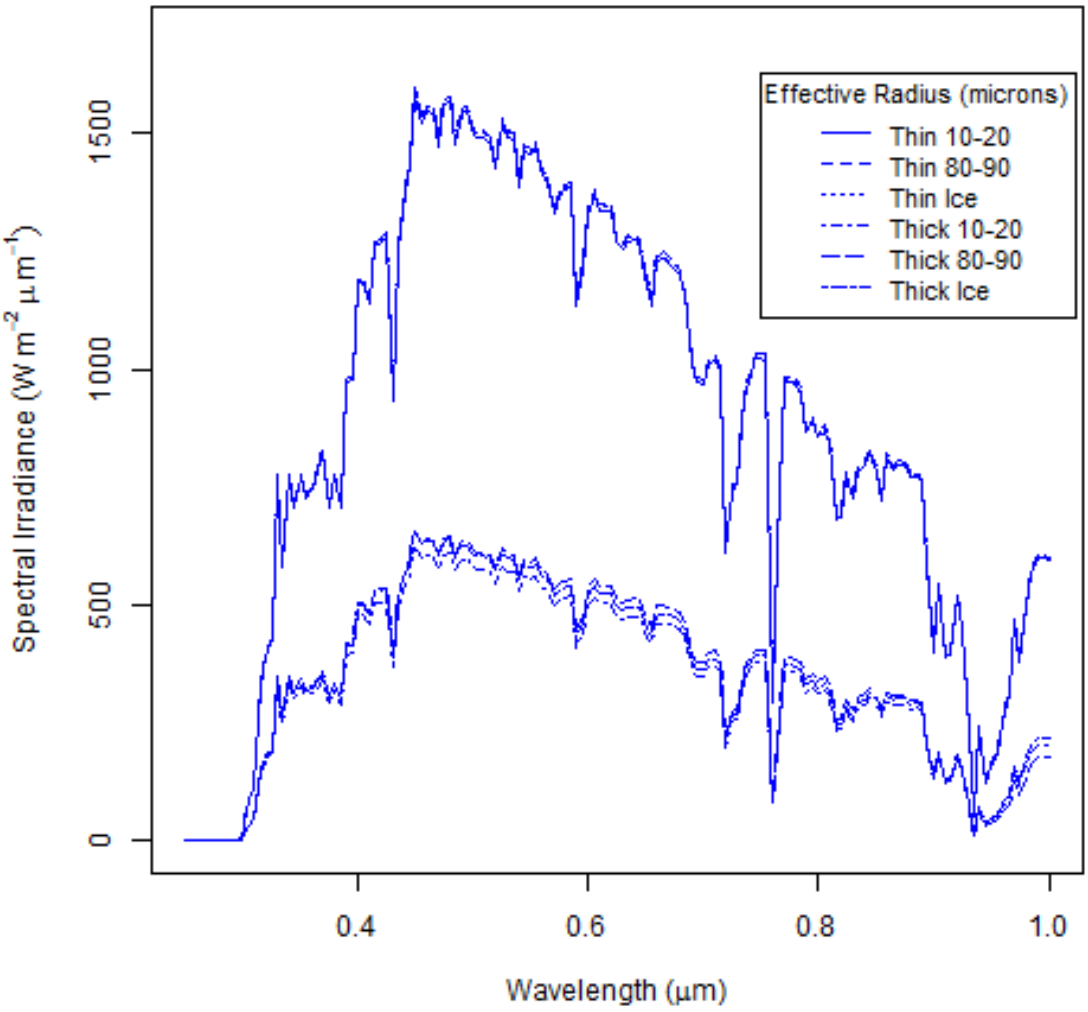

Figure 4.3. Downwelling spectral irradiance at the surface for thin high and thick high clouds with effective radii from 10-20 μm, 80-90 μm, and 10-20 μm ice phase.

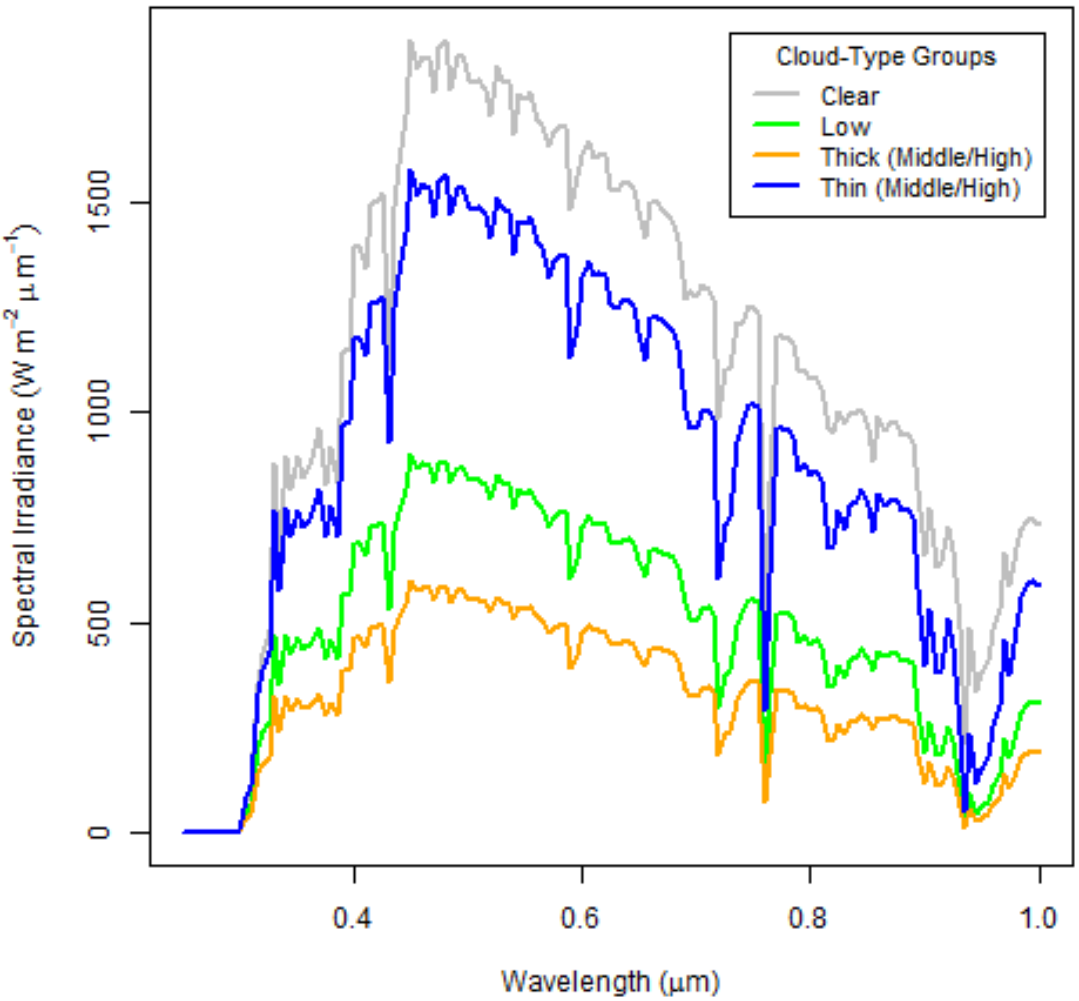

Figure 4.4. Downwelling spectral irradiance at the surface for cloud-type groups.

Table 4.2. Summary of mean downwelling shortwave spectral irradiance and surface radiation for cloud type sensitivity test runs.

Cloud-Type Group	**Mean Spectral Irradiance** ($Wm^{-2}\mu m^{-1}$)	**Surface Radiation** (Wm^{-2})
Low	486.0	366.9
Thin-Middle	879.2	663.8
Thick-Middle	318.2	240.2
Thin-High	879.6	664.1
Thick-High	319.0	240.8

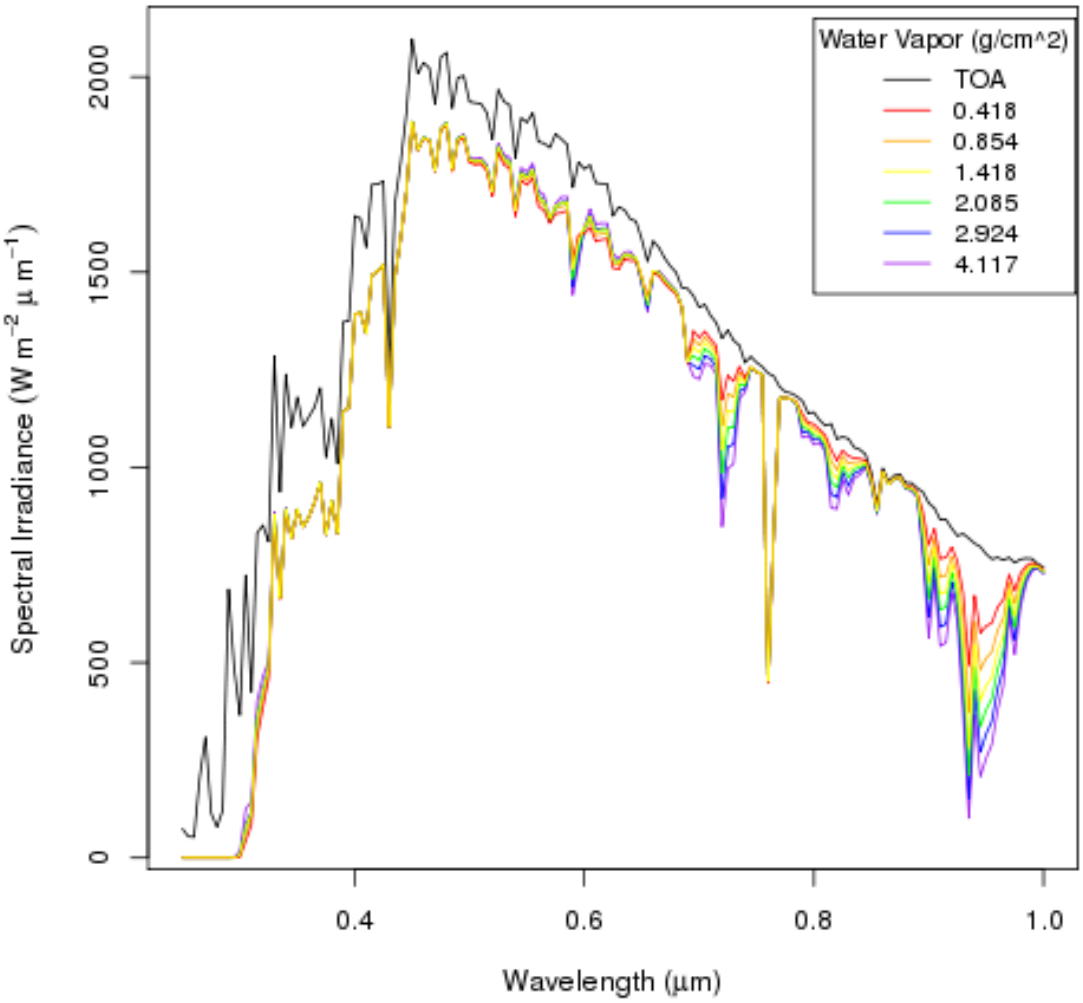

Figure 4.5. Downwelling spectral irradiance at the surface for variable atmospheric water vapor concentrations.

Table 4.3. Summary of mean downwelling radiometric quantities for water vapor concentration sensitivity test runs.

IDATM	**Precipitable Water Vapor** (gcm^{-2})	**Surface Radiation** (Wm^{-2})
Sub-arctic Winter	0.418	843.7
Mid-latitude Winter	0.854	838.9
US62	1.418	834.4
Sub-arctic Summer	2.085	828.3
Mid-latitude Summer	2.924	822.1
Tropical	4.117	817.3

considering the numerical differences in irradiance associated with cloud optical thickness and water vapor concentration, clouds appear to have a substantially greater influence. It cannot be stressed enough that the context of these results depends on the final application. In the case of subsequent analyses, water vapor does not influence surface radiation and subsequent pavement temperatures in a manner comparable to cloud cover.

b. Distribution Analysis of Clouds Versus Pavement Temperature

Time series plots of pavement temperature are produced in which observations are color-coded based on the modal cloud. Box plots separated by cloud-type groups show the pavement temperature distribution for each cloud-type group throughout the entire data set. In order to remove the diurnal trend and time dependence of pavement temperature, distribution analyses and cloud-type group comparisons are performed for specific time stamps throughout multiple days as well.

The June 2011 pavement temperature distributions by cloud-type group (Figure 4.6) are similar to those of the 1-16 June 2011 distributions (Figures 4.7 and 4.8). This result suggests that, despite variations in sample size between the whole month and first two weeks, there is some regular effect of cloud cover on pavement temperature (Table 4.4). Further, the similarities of these two data sets supports use of the two week data for more detailed analyses.

For both the June 2011 data and 1-16 June 2011 data, the low cloud-type group is in the middle for pavement temperature and had one of the largest interquartile ranges (IQR). The June 2011 mean pavement temperature for low clouds is 32.1 °C with the

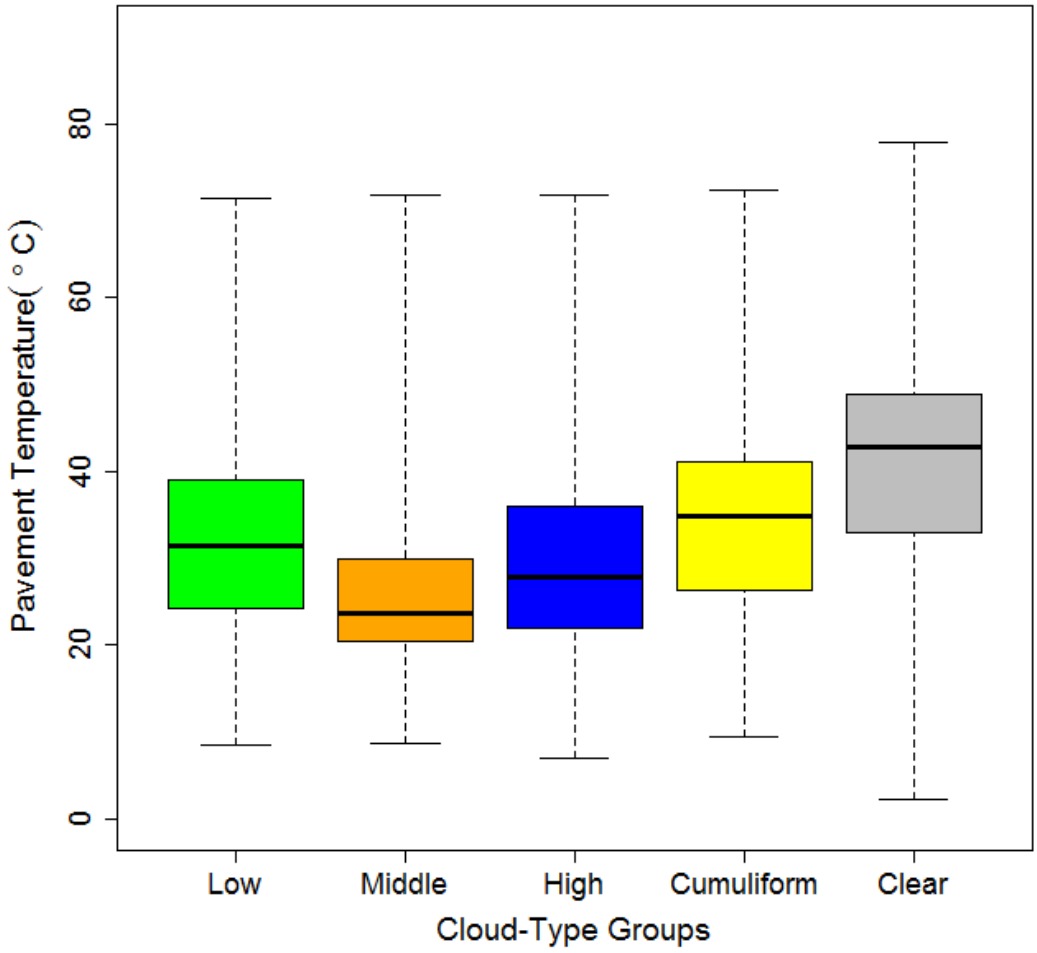

Figure 4.6. June 2011 road pavement temperature distributions sorted by cloud-type groups; low (green), middle (orange), high (blue), cumuliform (yellow), and clear (gray). The whiskers represent the extremes for the data (i.e., minimum and maximum), the box represents the first and third quartiles, and the median is the solid black bar in the middle of each box.

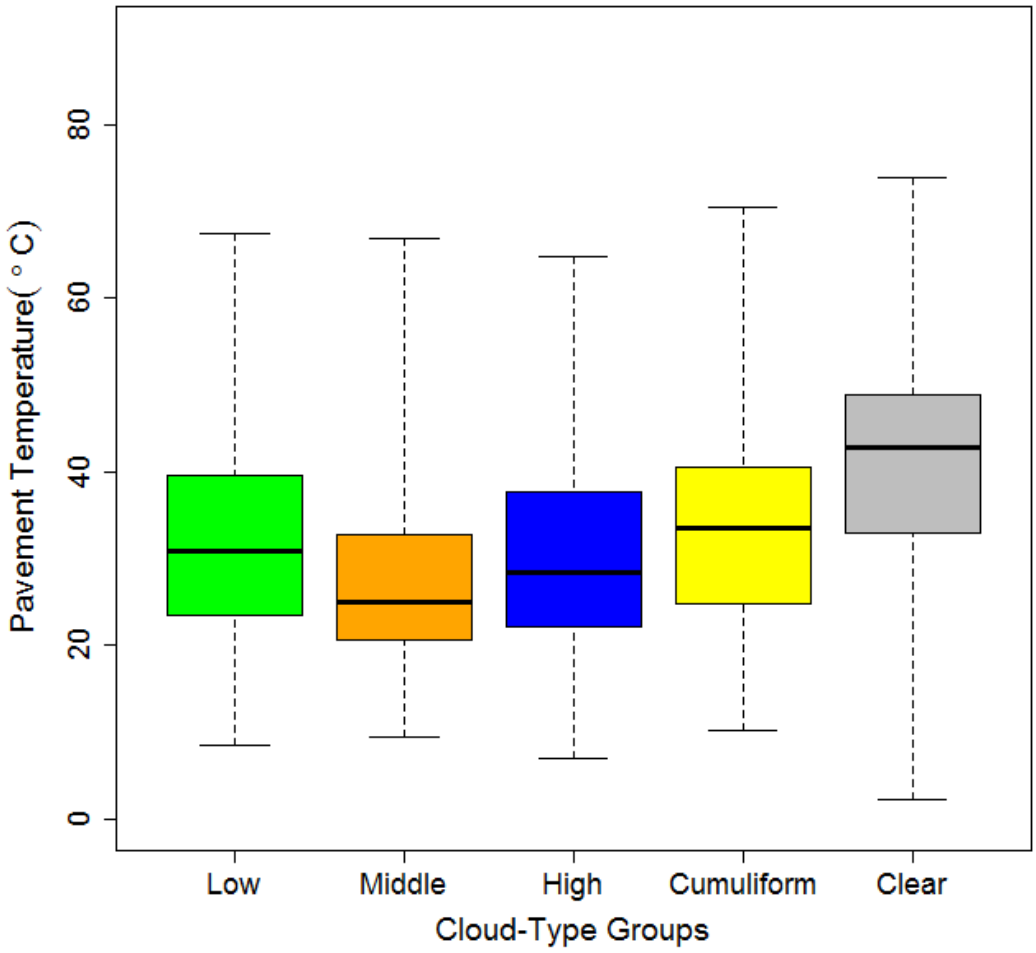

Figure 4.7. Road pavement temperature distributions from 1-16 June 2011 sorted by cloud-type groups; low (green), middle (orange), high (blue), cumuliform (yellow), and clear (gray). The whiskers represent the extremes for the data (i.e., minimum and maximum), the box represents the first and third quartiles, and the median is the solid black bar in the middle of each box.

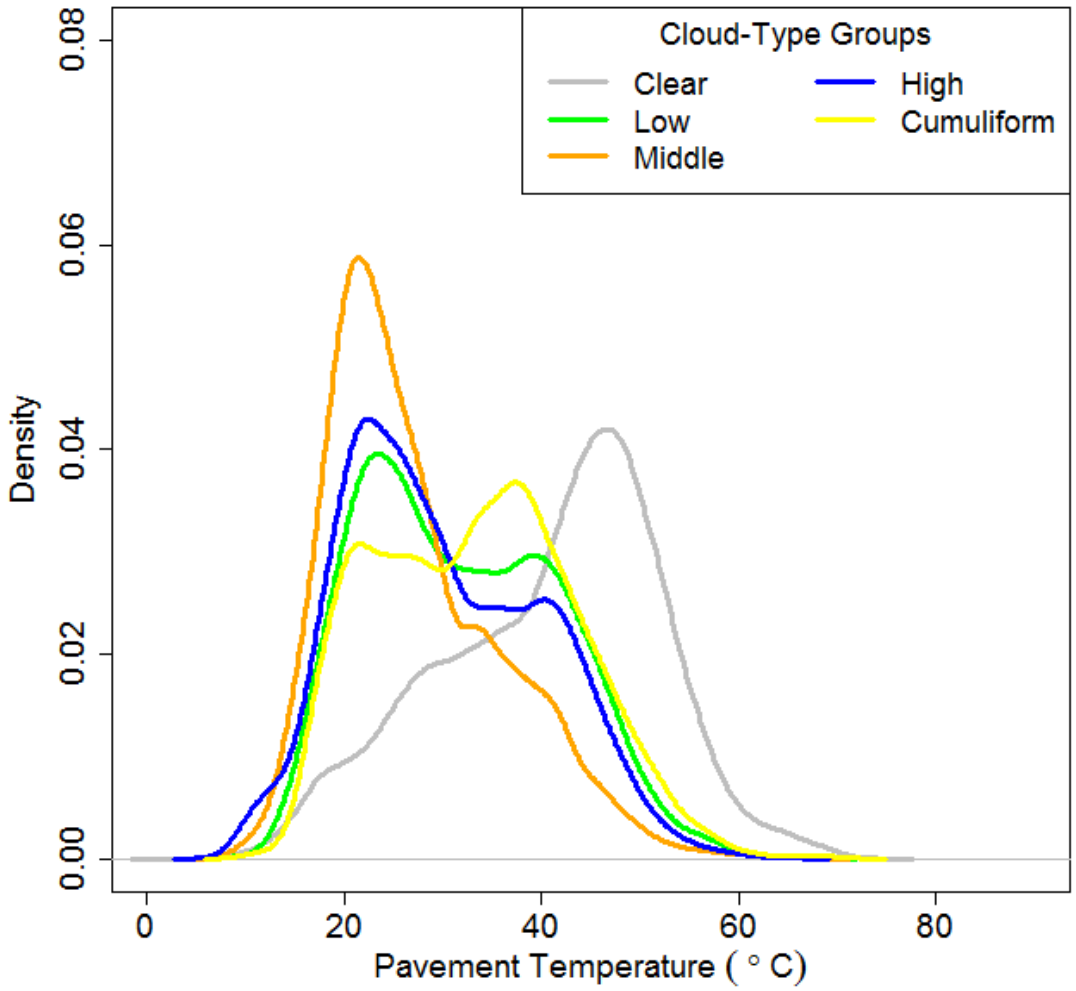

Figure 4.8. Gaussian kernel density distribution for 1-16 June 2011 pavement temperatures colored by cloud-type group.

Table 4.4. June 2011 and 1-16 June 2011 pavement temperature distribution analyses results.

Cloud-Type Group	Number of Observations	Mean Road Temp. (°C)	Median Road Temp (°C)	Interquartile Range (IQR) (°C)
		June 2011		
Low	11603	32.1	31.5	14.8
Middle	10638	25.8	23.7	9.5
High	18492	29.4	27.9	14.1
Cumuliform	18470	34.2	34.9	14.8
Clear	51852	40.9	42.8	15.9
		1-16 June 2011		
Low	8530	31.8	30.9	16.2
Middle	5755	27.1	25.0	12.1
High	12059	30.0	28.4	15.7
Cumuliform	10520	33.3	33.5	15.6
Clear	36781	40.8	42.9	16.0

second largest IQR of 14.8 °C. From 1-16 June, the mean pavement temperature for low clouds adjusted slightly downward to 31.8 °C and had the largest IQR of 16.2 °C. Low clouds (i.e., stratus and stratocumulus) tend to occur most often in the morning associated with morning fog, though they are also associated with precipitation during the day as well. This result makes sense when considering the already high temperatures associated with the month of June.

The middle cloud-type group contained the lowest pavement temperature observations for both June 2011 and 1-16 June 2011. The June 2011 mean pavement temperature for middle clouds is 25.8 °C and the 1-16 June 2011 mean is 27.1 °C. The IQR for middle clouds is 9.5 °C and 12.1 °C, respectively. Middle cloud-type groups (i.e., altostratus and altocumulus) tend to be spatially uniform. The smallest IQR for both the June 2011 and 1-16 June 2011 data are indicative that these clouds tend to have a less variable effect on pavement temperatures.

After middle clouds, high clouds contained the second lowest observed pavement temperature which is somewhat unexpected. The June 2011 mean pavement temperature for high clouds is 29.4 °C with an IQR of 14.1 °C. The 1-16 June 2011 mean pavement temperature is 30.0 °C with an IQR of 15.7 °C. One might expect that given the relatively thin characteristics of the high cloud-type group (i.e., cirrus, cirrostratus and cirrocumulus), pavement temperature would more closely resemble those of clear skies. This could be indicative of an important limitation of satellite-derived cloud observations. Cirrus clouds are the most likely group to be detected as they are the highest clouds in the atmosphere. Downward viewing satellites may be unable to detect other cloud-type groups below a cirrus canopy. It is suggested that while some of the observed high cloud

observations are truly only cirrus clouds, other situations are more suggestive of multiple layers of clouds and only the cirrus layer is detected.

The cumuliform cloud-type group presents a challenge of its own due to the scattered nature of the clouds. Cumuliform clouds contained the second highest pavement temperatures after clear sky conditions with an June 2011 mean of 34.2 °C (IQR of 14.8 °C) and 1-16 June 2011 mean of 33.3 °C (IQR of 15.6 °C). The cumuliform cloud-type group (i.e., cumulus, cumulus congestus, cumulonimbus and cirrus anvil associated with deep convection) contains some of the most complicated cloud situations. Fair weather cumulus clouds can be very scattered in nature shading only some regions from direct sunlight whereas deep convective clouds can be spatially broad and opaque to sunlight yielding cooler pavement temperatures especially when considering the complexity added by precipitation on the road surface. This combination of factors explains why the cumuliform cloud-type group exhibits the second highest pavement temperature and one of the larger IQR.

As expected, clear pavement temperatures are the highest with a June 2011 mean of 40.9 °C and 1-16 June 2011 mean of 40.8 °C. The IQR is 15.9 °C and 16.0 °C, respectively. Given the time of year, high pavement temperatures are expected. The important distinction to note is that clear pavement temperatures range anywhere from 6 °C-15 °C higher than their cloud counterparts. Extrapolate this difference to a wintertime scenario in which increasing or decreasing cloud cover could have substantial ramifications for a pavement temperature forecast with the threat of frozen precipitation.

For the 1-16 June 2011 period, another method to compare pavement temperature distributions by cloud-type group is with a probability density (Figure 4.8). At lower pavement temperatures there is a greater density, and therefore higher probability, of a particular observation being associated with cloud cover. At higher pavement temperatures, there is a greater propensity for clear observations. It is also important to note that cloud cover pavement temperature distributions do appear to be somewhat bimodal with a weaker, secondary peak occurring at higher temperatures. This is likely due to the time of day at which any given cloud-type group occurs. Cloud cover during the peak solar heating of any given day will still yield higher pavement temperatures than say an early morning or late evening cloud cover. This bimodal nature is substantially more apparent in the cumuliform cloud-type group which agrees with the aforementioned discussion of how this group represents the most complex cloud situations. Lower pavement temperatures with cumuliform clouds are likely associated with deep convection. Higher pavement temperatures with the same cloud-type group are more likely to occur in situations with fair weather, scattered cumulus clouds. This cloud-type group has a higher probability of such split observations.

The pavement temperature distributions of the three select case days (Figures 4.9-4.11) introduce more variability and complexity into the analysis which is expected given the fact that no two cloudy days are alike. These three case days are primarily identified for the purposes of later assessing reliability of the NRLCC algorithm; however, their pavement temperature distributions also emphasize the importance of accounting for the diurnal dependence of temperature. Recall that 1 June 2011 is defined as a partly cloudy day. The pavement temperature distributions by cloud-type group are

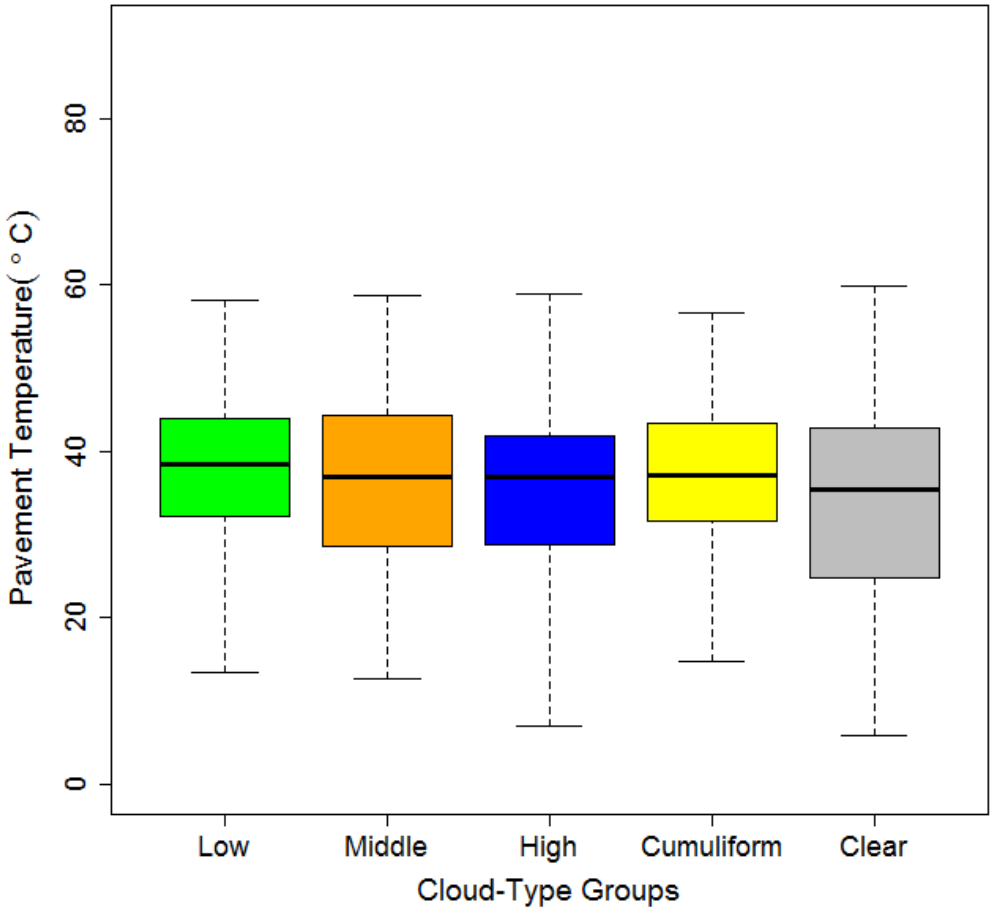

Figure 4.9. Pavement temperature distribution from 1 June 2011 (partly cloudy day) sorted by cloud-type groups; low (green), middle (orange), high (blue), cumuliform (yellow), and clear (gray). The whiskers represent the extremes for the data (i.e., minimum and maximum), the box represents the first and third quartiles, and the median is the solid black bar in the middle of each box.

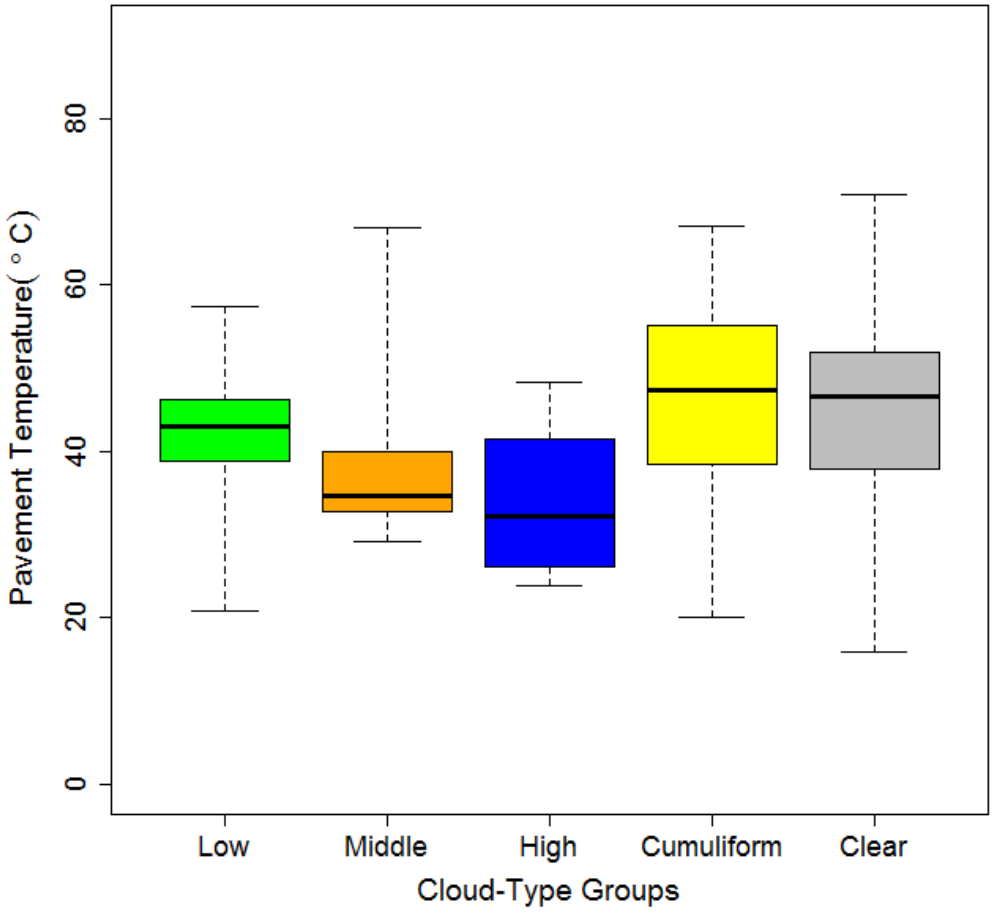

Figure 4.10. Pavement temperature distributions on 6 June 2011 (clear day) sorted by cloud-type groups; low (green), middle (orange), high (blue), cumuliform (yellow), and clear (gray). The whiskers represent the extremes for the data (i.e., minimum and maximum), the box represents the first and third quartiles, and the median is the solid black bar in the middle of each box.

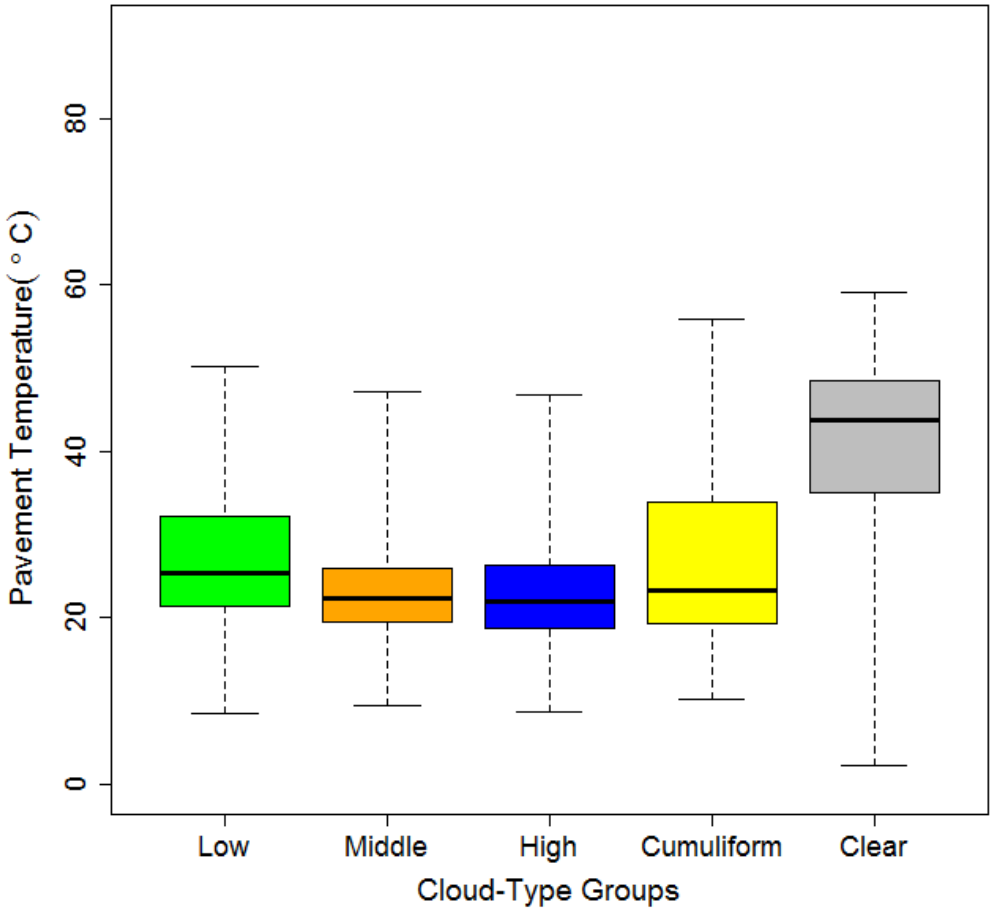

Figure 4.11. Pavement temperature distribution on 9 June 2011 (cloudy day) sorted by cloud-type groups; low (green), middle (orange), high (blue), cumuliform (yellow), and clear (gray). The whiskers represent the extremes for the data (i.e., minimum and maximum), the box represents the first and third quartiles, and the median is the solid black bar in the middle of each box.

nearly identical in terms of both their variation and medians (Figure 4.9). This result seems anomalous as clear pavement temperatures in the June 2011 data set are substantially higher than those of cloudy temperatures. A further complication is apparent during the clear day on 6 June 2011 (Figure 4.10) in which there is more realistic variation among the pavement temperature observations of the cloudy versus clear situation. The median of the cumuliform cloud-type group is higher than that of clear conditions which again deviates from the tendencies of the June 2011 data set. One final disagreement between the case days and the entire month data set to note is on the distribution on the cloudy case day of 9 June 2011 (Figure 4.11). The disagreement here originates from a consideration of the distribution of clear pavement temperatures here compared to clear pavement temperatures of the clear day. These three pavement temperature distributions suggest that to consider the daily variability in pavement temperature when grouped by cloud cover is not an appropriate means to illustrate the variation in pavement temperature associated with cloud cover. The best accommodation is to remove the time dependence from the data and consider the pavement temperatures by cloud-type groups at specific TODs.

The TOD distribution analyses (Figures 4.12 and 4.13, Table 4.5) best illustrate the impact of the cloud-type groups on pavement temperatures. Recall the five key TODs that were defined; sunrise (12 UTC), morning (15 UTC), midday (18 UTC), afternoon (21 UTC) and sunset (00 UTC). A discussion of the tendencies of pavement temperature cloud-type groups at each time step allow for quantification of the impact of cloud type on pavement temperature (Figure 4.12). At 12 UTC, or approximately sunrise, the lowest daytime temperatures are observed for all groups. Further, the variation and median

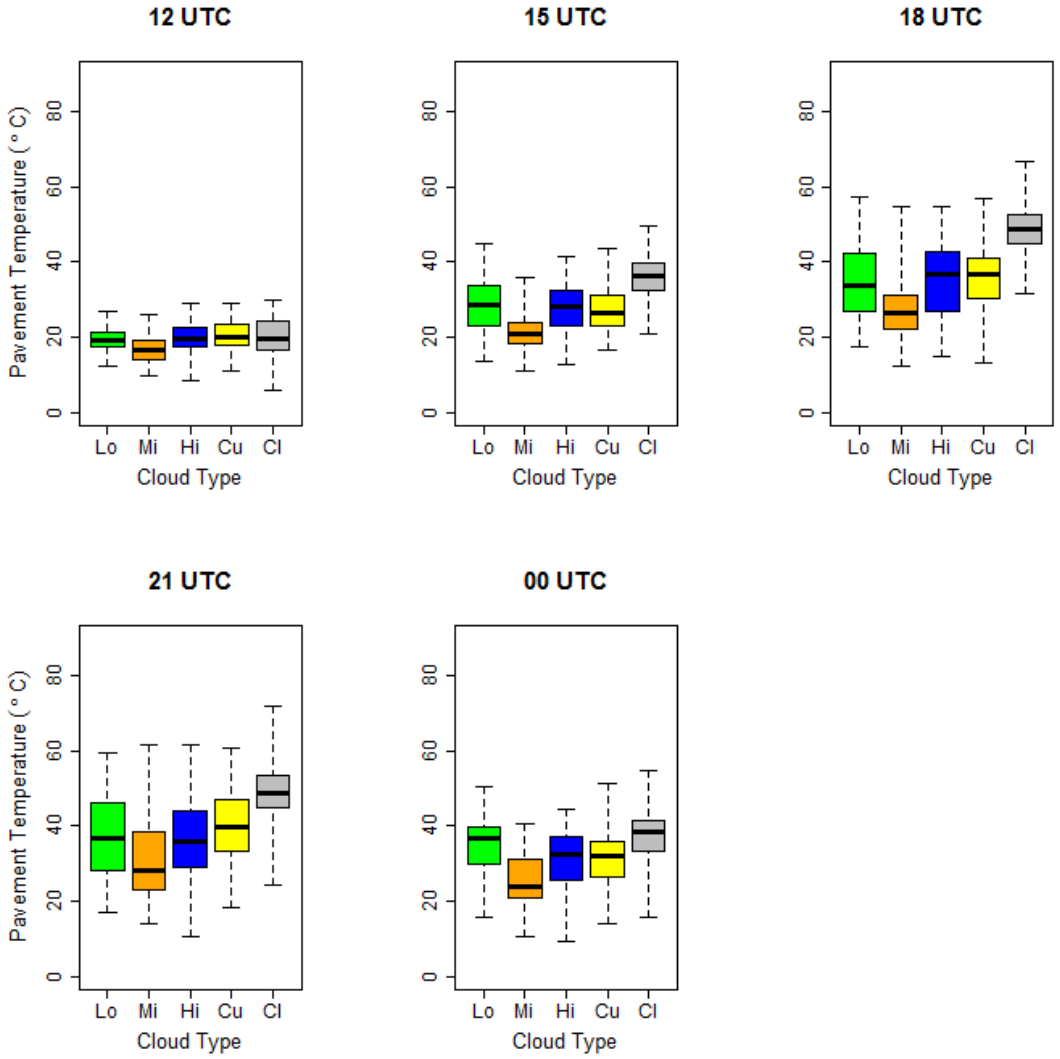

Figure 4.12. Time of day (TOD) pavement temperature observation distributions for 1-16 June 2011 stratified by cloud-type groups; low (green), middle (orange), high (blue), cumuliform (yellow), and clear (gray). 12 UTC represents approximate sunrise, 15 UTC is a morning observation, 18 UTC represents the middle of the day in which typical peak solar heating occurs, 21 UTC is the afternoon and 00 UTC represents approximate sunset. The whiskers represent the extremes for the data (i.e., minimum and maximum), the box represents the first and third quartiles, and the median is the solid black bar in the middle of each box.

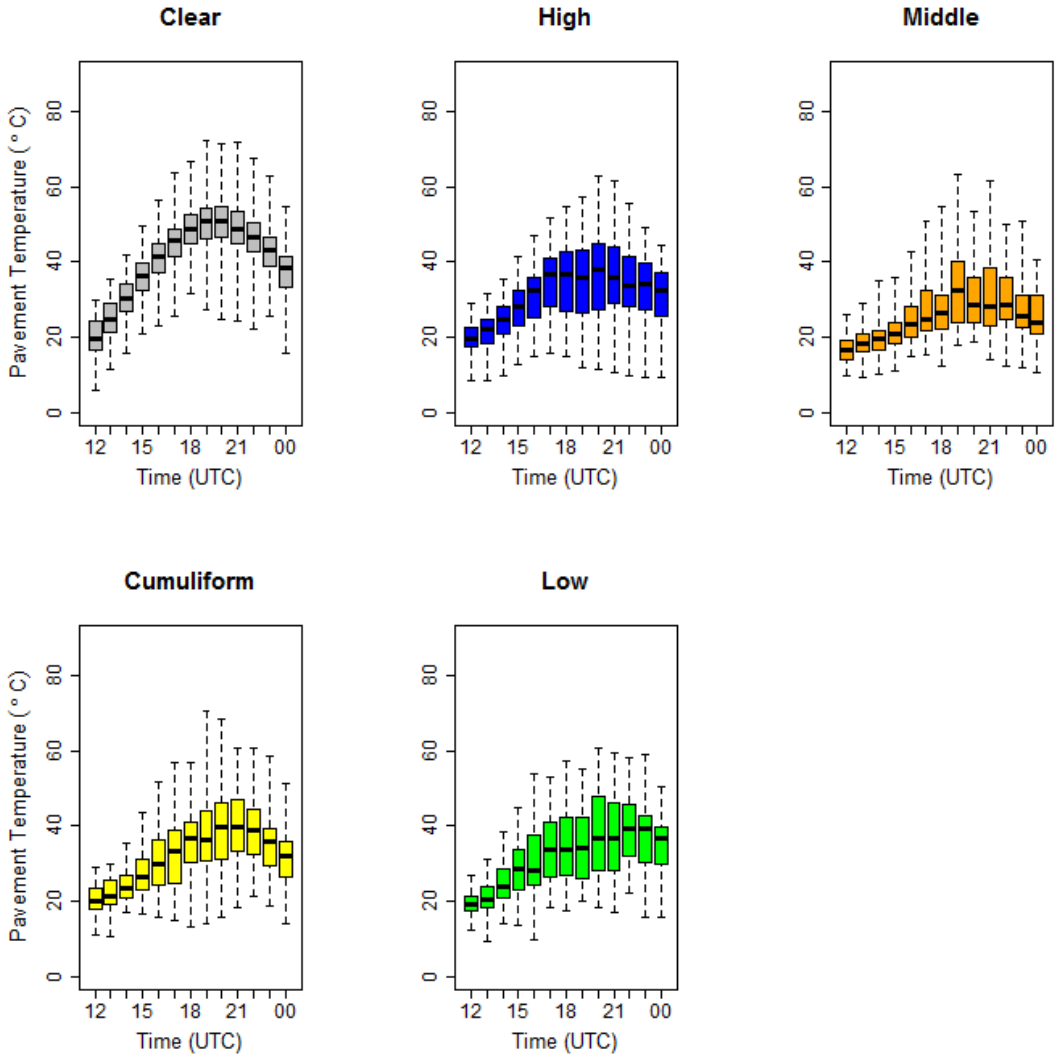

Figure 4.13. Hourly pavement temperature distributions for the 1-16 June 2011 period sorted by cloud-type groups. The whiskers represent the extremes for the data (i.e., minimum and maximum), the box represents the first and third quartiles, and the median is the solid black bar in the middle of each box.

Table 4.5. Time of day (TOD) pavement temperature distribution analyses results from 1-16 June 2011 with median, interquartile range (IQR) and mean pavement temperatures given.

		Time (UTC)												
	Road Temp (°C)	12	13	14	15	16	17	18	19	20	21	22	23	00
Low	Median	19.0	20.5	23.8	28.6	28.0	33.9	33.9	34.0	36.7	36.8	39.2	39.3	36.9
	IQR	3.9	5.6	7.7	11.0	13.4	14.6	15.4	16.5	19.2	17.8	13.7	12.7	9.9
	Mean	19.3	20.9	24.9	28.5	30.6	33.8	35.1	34.7	38.0	36.8	38.9	36.6	35.1
Middle	Median	16.8	18.4	19.7	21.0	23.5	24.9	26.3	32.7	28.6	28.3	28.5	25.8	23.8
	IQR	4.8	4.9	5.2	5.7	8.1	10.6	8.9	16.0	11.9	15.5	11.3	8.2	9.9
	Mean	16.9	18.7	19.8	21.5	24.9	27.0	27.5	32.9	30.5	31.0	30.4	27.7	25.4
High	Median	19.8	22.0	24.7	28.1	32.4	36.8	36.9	36.1	37.9	36.1	33.9	34.2	32.7
	IQR	5.4	6.3	7.5	9.4	10.8	13.0	15.6	16.8	17.5	14.9	13.4	12.7	11.8
	Mean	19.6	21.5	24.3	27.8	31.2	34.9	35.2	35.0	36.5	36.1	34.2	33.5	31.5
Cumuli.	Median	20.0	21.4	23.4	26.4	29.9	33.5	36.7	36.3	39.8	39.9	38.7	36.0	31.9
	IQR	5.4	6.2	5.9	8.1	11.8	13.9	10.8	13.1	15.0	13.5	11.5	10.0	9.7
	Mean	20.6	22.1	24.1	27.1	30.3	32.5	35.2	36.8	38.4	39.5	38.4	34.7	31.6
Clear	Median	19.8	24.9	30.5	36.5	41.4	45.9	49.0	50.8	50.7	48.9	46.7	43.3	38.3
	IQR	7.8	7.7	7.2	7.4	7.6	7.5	7.9	8.0	8.4	8.5	7.8	7.7	8.1
	Mean	19.9	24.7	30.0	35.7	40.9	45.5	49.0	50.5	50.9	49.4	47.0	43.2	37.5

pavement temperatures are very similar. This result is suggestive that near the day/night transition, the variability in pavement temperature associated with cloud cover is at quasi-equilibrium. This quasi-equilibrium is an illustration of the radiative balance between shortwave radiation and longwave radiation that occurs near the day/night transition. At sunrise, the longwave emission cooling pavement temperatures is balanced by the shortwave radiation that is only beginning to induce warming.

Moving ahead to 15 UTC (morning), the solar zenith angle decreases (i.e., sun rises higher in the sky) and the pavement temperatures for cloud-type groups begin to differentiate between clear versus cloud. Clear conditions, not surprisingly, observed the most rapid increases in pavement temperatures of 16.7 °C between the two TOD (Table 4.5). The four cloud-type groups increased in temperature as well, but there was a clear reduction in the magnitude of increase. Low cloud pavement temperatures observed the second highest increase of 9.6 °C, followed by high cloud pavement temperatures with 8.3 °C; cumuliform cloud-type group at 6.4 °C and middle cloud pavement temperature observations increased the least with only a 4.2 °C increase in the median.

Peak solar heating typically occurs around midday (18 UTC) although the highest pavement temperatures should occur after this TOD (Table 4.5). The lagged response of the pavement temperature to solar heating is associated with the specific heat capacity of the atmosphere, various road surfaces and the fact that the surface remains exposed to warming for several hours after peak solar heating. Substantial energy is required to affect the sensible heat of any given material such as a road. From the morning to midday period clear-sky pavement temperatures increased another 12.5 °C. The cumuliform cloud-type group observed the second largest increase of 10.3 °C followed by the high

cloud-type group at 8.8 °C. The lowest increases between the two TOD are associated with both the low and middle cloud-type groups at 5.3 °C.

The afternoon period (21 UTC) generally observed the highest median pavement temperatures associated with all cloud-type groups and relatively small increases from the midday TOD (Table 4.5). The median afternoon pavement temperature for clear conditions was 48.9 °C which is a decrease of 0.1 °C from midday. The second highest median afternoon pavement temperature is associated with the cumuliform cloud-type group of 39.9 °C which represents a 3.2 °C increase from midday. This observation is followed by the low cloud-type group with an observed afternoon median of 36.8 °C which is an increase from midday of 3.0 °C. High cloud-type group median pavement temperatures in the afternoon are 36.1 °C which was a decrease of 0.8 °C from the midday TOD. Middle clouds remain the coolest cloud-type group of the day with an afternoon median pavement temperature of 28.3 °C which is an increase of 2.1 °C from midday. One possible reason for the increase in pavement temperatures associated with cloud cover and decrease for clear-sky pavement temperatures is that clouds impede both longwave and shortwave radiation from traversing into space. Cloud cover will act to keep pavement temperatures cooler than clear-sky pavement early in the day and then will act to keep pavement temperatures slightly elevated later in the day.

The final time sunset TOD (00 UTC) is a decrease for all pavement temperature cloud-type groups. Just as quickly as it climbed, pavement temperatures associated with clear conditions cool rapidly as well with an afternoon to sunset decrease of 10.6 °C. Pavement temperature observations under the cumuliform cloud-type group cooled the second most rapid with a median decrease of 8.0 °C. This is followed by middle clouds at

4.6 °C and high clouds at 3.4 °C. Low clouds observe a slight increase of 0.1 °C from the afternoon TOD to the sunset TOD, which essentially represents no change. These results are likely associated with the fact that cloud cover damps the diurnal pavement temperature cycle. Pavement temperatures early in the day are kept cooler whereas later in the day the pavement does not cool as quickly due cloud cover insulating surface radiation.

Hourly pavement temperature distribution observations allow for an increase in the temporal resolution to consider the differences among the pavement temperature cloud-type groups (Figure 4.13 and Table 4.5). The position of each cloud-type group is deliberate to suggest the cumuliform cloud-type group exhibit a hybrid tendency of clear and cloud conditions and the remaining cloud-type groups are most closely attributed with pure cloud cover observations. Clear pavement temperatures have the least within-period variation throughout the day and the most between-period variations. This is due to the fact that surface radiation is not impeded by cloud cover for the clear-sky pavement. Clear median pavement temperatures change rapidly with solar heating. Cumuliform and low cloud-type groups both exhibit reductions in pavement temperature from clear-sky pavement and also the largest within TOD variability. High cloud-type group observed pavement temperatures are lower than those of cumuliform and low cloud-type groups. Middle clouds observe the coolest and most damped diurnal median pavement temperature tendencies. These apparent relationships suggest some of the governing principles associated between cloud cover and pavement temperatures. As noted in the SBDART model sensitivity analysis, cloud optical thickness, rather than cloud height, or layer thickness, is the primary parameter of influence to radiative

transfer. The pavement temperature TOD distributions reveal similar tendencies. Given the nature of the middle cloud-type group (i.e., altocumulus and altostratus) these tend to be some of the more optically thick clouds. Further, the middle cloud-type group tends to produce more of a uniform cloud deck over a given region. The high cloud-type group tends to be optically thinner in nature and so the pavement temperature response to this cloud-type group is not as severe as with that of the middle group. The cumuliform and low cloud-type groups contain the largest within-TOD variability due to the nature of these clouds. The cumuliform cloud-type group contains generally optically thick clouds; however, they may be very sparse and scattered in nature (e.g., fair weather cumulus clouds) or quite dense (deep convective cumulonimbus clouds). A similar statement is applicable to the low cloud-type group which may contain relatively optically thin stratus (i.e., fog) or widely scattered stratocumulus. Optically thicker clouds in the same low cloud-type group could be a denser and uniform layer of stratus clouds such as those associated with precipitation. These pavement temperature distributions represent the first time that satellite cloud data are used to develop cloud-type groups that can be associated with pavement temperature observations.

A time series of median pavement temperature observations (Table 4.5) colored by cloud-type groups (Figure 4.14) is produced to serve as a corollary to the probability density series (Figure 4.8). The median time series exhibits a clear distinction between cloudy conditions and clear conditions. Among the four cloud-type groups, the middle cloud has the most distinct median time series from the remaining cloud-type group. This signifies that the radiative properties of such clouds groups are important to model distinctly rather than grouping all clouds together. It could be suggested that a similar

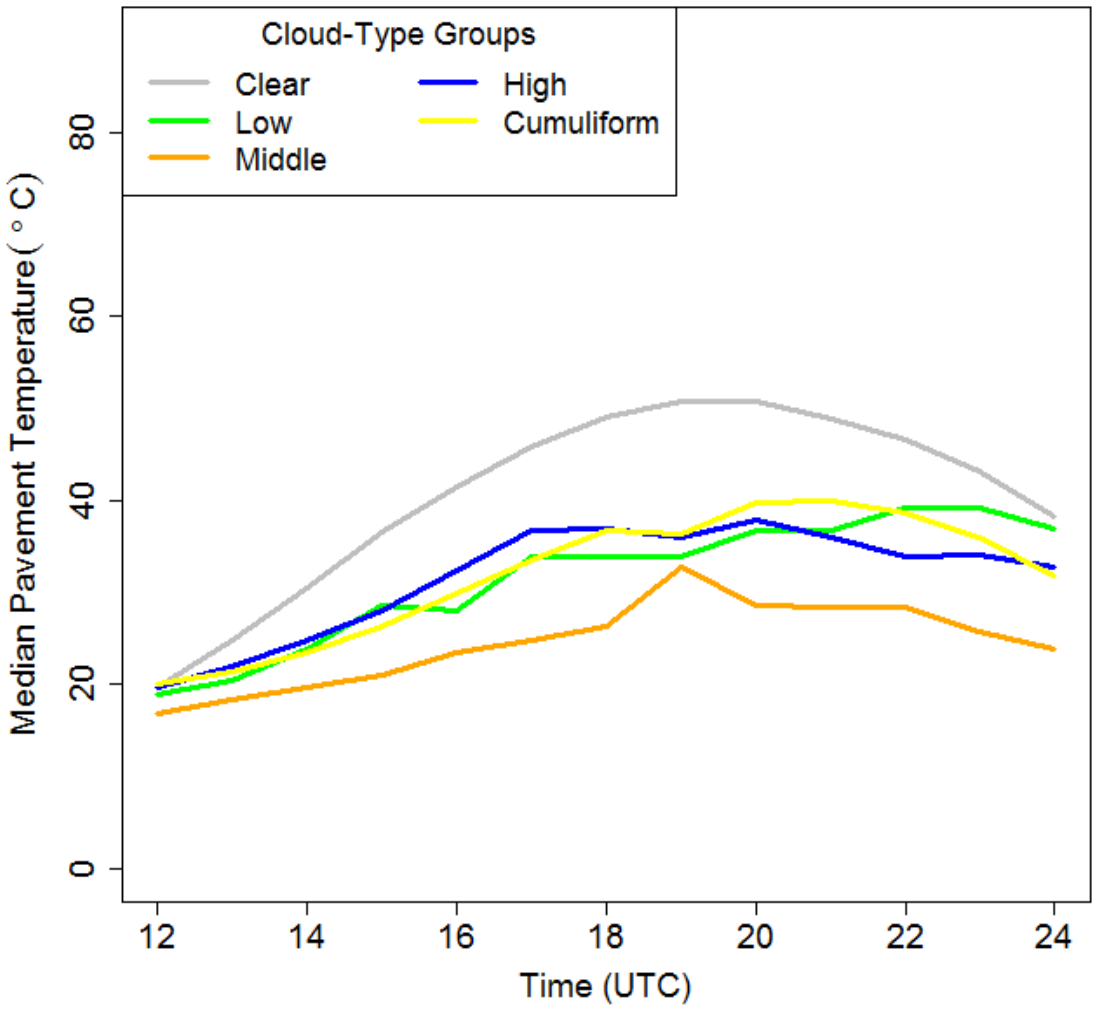

Figure 4.14. Hourly 1-16 June 2011 median pavement temperature observations colored by cloud-type groups.

model may be appropriate for the cumuliform, low and high cloud-type groups combined, although distinct models are more appropriate given apparent TOD variability. The cloud-type groups begin the day with little difference, but conclude the day with clear separation in the median time series.

c. Distributions and Correlations Among Clouds, Pavement Temperature and Radiation

The 1-16 June 2011 surface radiation distributions by cloud-type group (Figures 4.15 and 4.16, Table 4.6) are only performed for specific TODs and hourly unlike the pavement temperature distributions by cloud-type group for the entire period. The variation in radiation is substantially larger than that of pavement temperatures and an overall distribution comparison is not appropriate.

At 12 UTC, which recall is approximately sunrise, the surface radiation distributions are very similar with little variation (Figure 4.15) which correlates to the concept of the day/night transition equilibrium state that was also observed in the pavement temperatures as well. At this initial TOD clear conditions observe the highest median surface radiation of 185.5 Wm^{-2}, followed by the cumuliform cloud-type group with 120.0 Wm^{-2}, high clouds with 79.7 Wm^{-2}, middle clouds at 46.7 Wm^{-2}, and the lowest observed surface radiation was associated with low clouds at 39.6 Wm^{-2} (Table 4.6). These distributions are expected in that, while there is little surface radiation near sunrise, there already is some separation among clear and cloudy conditions.

Later in the morning at 15 UTC, there is substantially more division among the surface radiation distributions by cloud-type group (Figure 4.15). In the intervening three

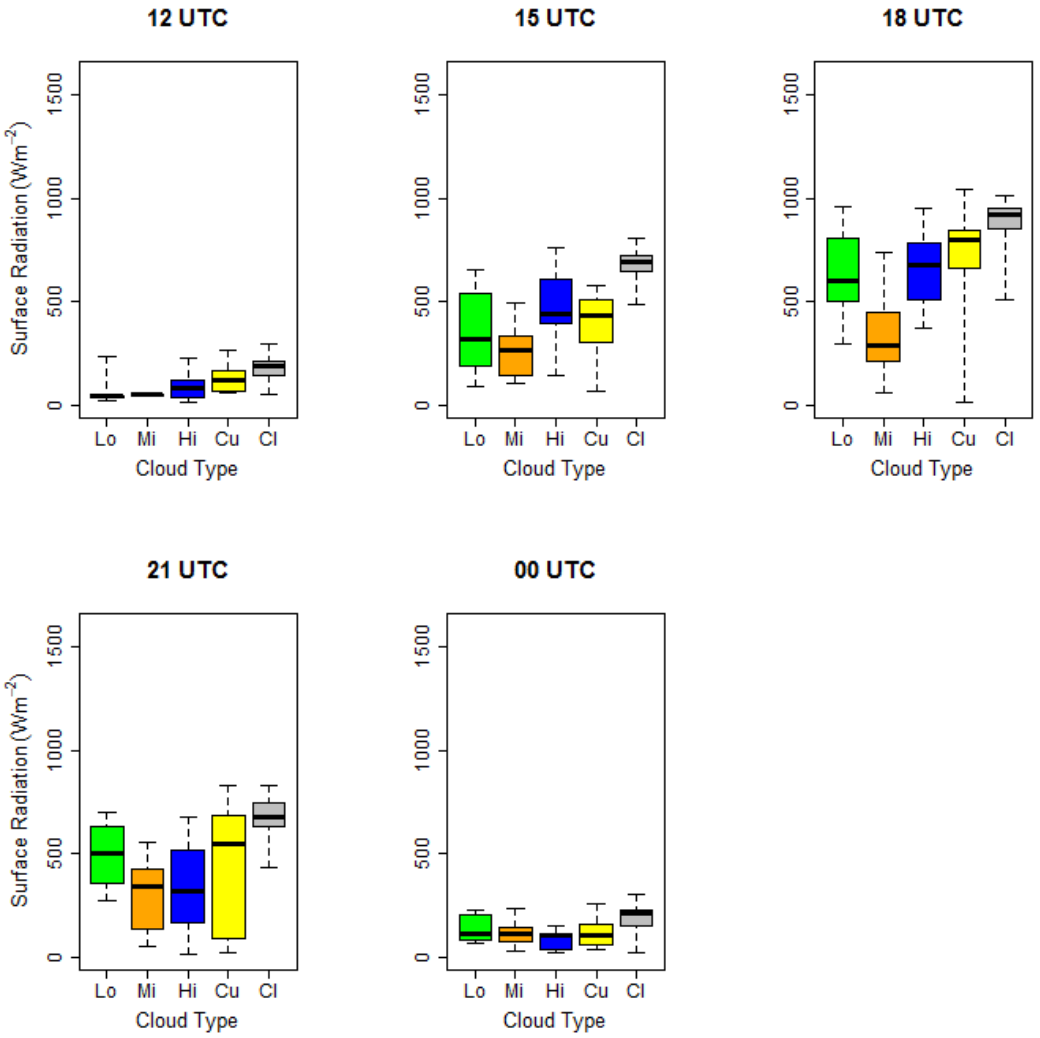

Figure 4.15. TOD surface radiation observation distributions from 1-16 June 2011 sorted by cloud-type groups; low (green), middle (orange), high (blue), cumuliform (yellow), and clear (gray). 12 UTC represents approximate sunrise, 15 UTC is a morning observation, 18 UTC represents the middle of the day in which typical peak solar heating occurs, 21 UTC is the afternoon and 00 UTC represents approximate sunset. The whiskers represent the extremes for the data (i.e., minimum and maximum), the box represents the first and third quartiles, and the median is the solid black bar in the middle of each box.

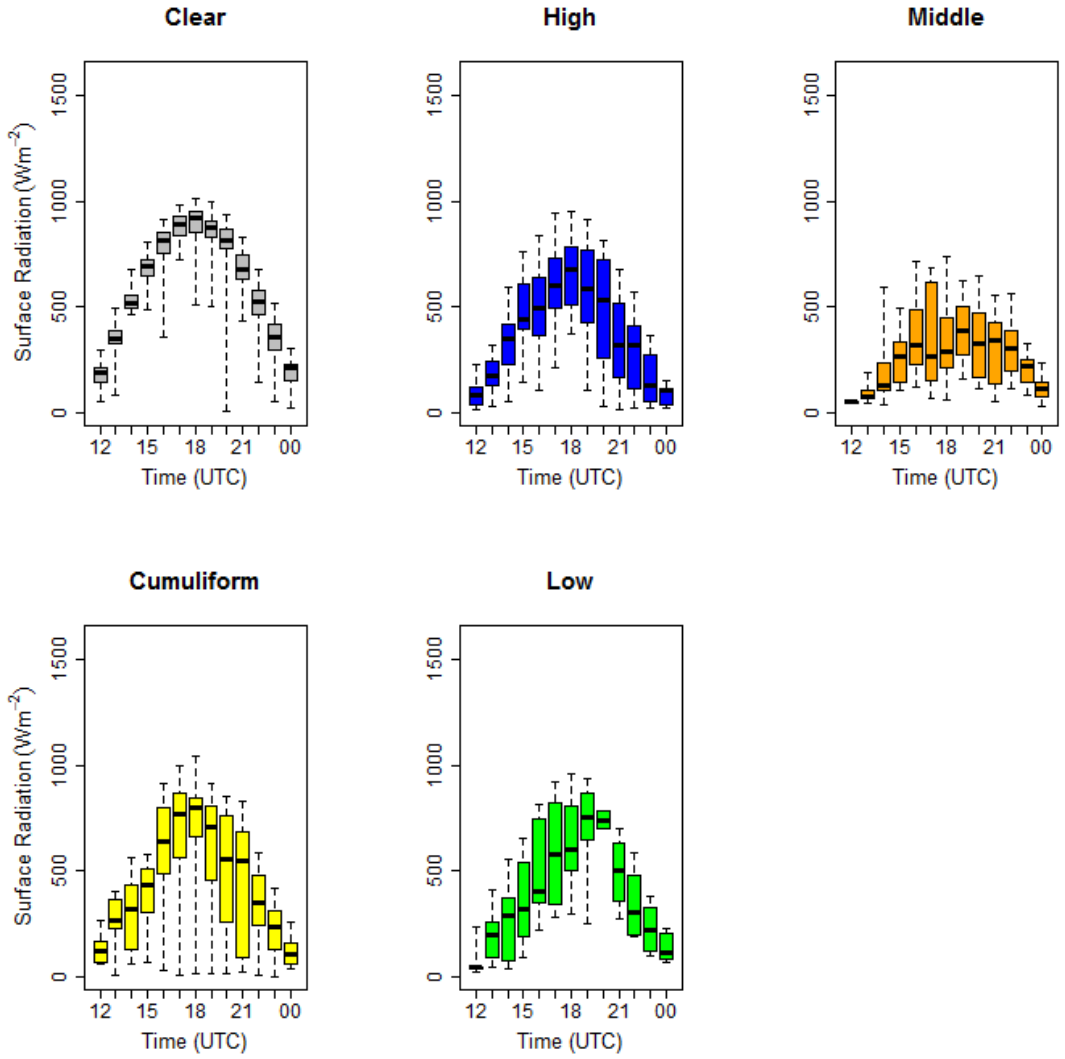

Figure 4.16. Hourly surface radiation observation distributions from 1-16 June 2011 arranged by cloud-type groups. The whiskers represent the extremes for the data (i.e., minimum and maximum), the box represents the first and third quartiles, and the median is the solid black bar in the middle of each box.

Table 4.6. Time of day (TOD) surface radiation distribution analyses results from 1-16 June 2011 with median, interquartile range (IQR) and mean surface radiation given.

		Time (UTC)												
	Surface Flux (Wm^{-2})	12	13	14	15	16	17	18	19	20	21	22	23	00
Low	Median	39.6	197.5	286.6	314.3	404.8	579.0	600.9	750.0	740.1	501.5	302.2	220.1	108.1
	IQR	14.1	170.0	282.8	351.3	396.6	415.0	306.6	221.1	41.25	206.3	282.9	207.8	119.7
	Mean	66.0	192.3	267.9	350.9	516.9	581.0	637.1	717.9	740.1	493.0	350.2	222.4	133.2
Middle	Median	46.7	76.2	129.6	266.9	319.0	265.0	285.6	388.4	322.8	338.1	300.7	219.8	109.4
	IQR	4.9	38.0	131.3	183.1	234.9	438.3	231.7	227.4	303.4	276.4	166.7	107.0	69.8
	Mean	47.9	86.4	186.3	252.1	360.9	356.9	343.6	386.5	338.4	302.7	304.0	201.9	117.2
High	Median	79.7	173.8	346.8	437.5	492.6	596.1	675.1	583.7	530.4	316.9	320.1	125.0	100.5
	IQR	80.9	114.0	192.8	207.9	254.2	231.6	274.3	346.4	438.1	346.6	297.5	204.1	76.4
	Mean	86.6	172.0	325.8	466.2	495.1	592.9	665.8	561.7	491.6	343.1	271.6	156.1	83.8
Cumuli.	Median	120.0	262.0	321.1	431.4	635.9	768.0	800.0	703.8	550.4	549.5	347.0	231.1	101.9
	IQR	91.9	134.7	295.9	205.4	314.6	291.6	185.0	341.4	505.4	564.7	218.8	150.6	88.3
	Mean	131.8	251.2	295.1	383.4	592.9	662.1	673.6	588.6	512.2	429.7	325.7	211.1	116.4
Clear	Median	185.5	351.4	518.3	690.1	812.2	890.6	919.0	876.3	811.0	677.6	520.6	358.3	208.1
	IQR	71.4	65.1	63.8	73.2	105.1	86.9	94.6	74.9	87.1	119.6	116.9	120.1	80.8
	Mean	181.2	353.2	530.8	685.1	790.6	878.0	891.8	865.3	797.2	675.2	505.8	345.0	190.1

hour period, the median surface radiation for clear conditions increased the most by 504.6 Wm^{-2}, to 690.1 Wm^{-2}. High clouds observe the second largest increase in median of 357.9 Wm^{-2}, moving up to 437.5 Wm^{-2}. The cumuliform cloud-type group observed a similar increase to that of high clouds with an increase of 311.4 Wm^{-2} to a median radiation of 431.4 Wm^{-2}. Low cloud radiation increased at a slower rate of 274.7 Wm^{-2} to a median of 314.3 Wm^{-2}. Middle clouds observed the smallest increase in radiation of 220.2 Wm^{-2} to a median observation of 266.9 Wm^{-2} (Table 4.6). These results are suggestive that the radiative influence of optically thin high clouds is similar to that of spatially scattered (albeit optically thicker) cumuliform clouds. Low and middle cloud-type groups tend to be both optically thicker and more spatially uniform and consistent, hence their lower observed median surface radiation.

Peak solar heating typically occurs around midday (18 UTC), although peak surface heating tends to lag. An important difference among the pavement temperature distributions and those for surface radiation is that peak radiation observations are much closer to peak solar heating (18 UTC through 19 UTC) whereas peak pavement temperatures were more likely to occur between 19 UTC and 21 UTC (Tables 4.5 and 4.6). In terms of radiation observation change from the previous three hour period, clear conditions observed the highest median radiation of 919.0 Wm^{-2} at the midday period, but not the greatest increase. Clear radiation increased 228.9 Wm^{-2} from the previous three hours. The cumuliform cloud-type group radiation observations increased the most by 368.6 Wm^{-2} to a second highest median of 800.0 Wm^{-2}. The third highest median radiation is associated with high clouds of 675.1 Wm^{-2} which is an increase of 237.6 Wm^{-2} from the previous three hours. Low clouds increase by 286.6 Wm^{-2} to a

median of 600.9 Wm^{-2}. From morning to midday, middle clouds only increase by 18.7 Wm^{-2} to a median of 285.6 Wm^{-2}. For middle clouds it is important to clarify that one hour later, at 19 UTC, the median radiation jumps markedly to 388.4 Wm^{-2} (Table 4.6). Similar to the tendencies in pavement temperature, surface radiation for clear conditions has the fastest increase in the morning while surface radiation under the cloud-type groups catches up during the midday period.

During the afternoon (21 UTC) surface radiation observations generally tend to decrease as solar zenith angle increases (Figure 4.15). Clear conditions decrease by 241.4 Wm^{-2}, though still maintain the highest median surface radiation of 677.6 Wm^{-2}. Cumuliform clouds decrease faster than clear conditions by 250.5 Wm^{-2} to a second highest median radiation of 549.5 Wm^{-2}. Low cloud-type group radiation values do not decrease as quickly, a loss of 99.4 Wm^{-2} to a median radiation of 501.5 Wm^{-2}. Middle clouds observe an increase of 52.5 Wm^{-2} in the three hour period to a median radiation of 338.1 Wm^{-2}. The high cloud-type group observes the most rapid decrease of 358.2 Wm^{-2} in the three hour period with an afternoon median radiation of 316.9 Wm^{-2} (Table 4.6). Such a rapid decrease with such a relatively optically thin cloud-type group seems anomalous. One possible explanation is that the NRLCC algorithm only provides a classification for the highest cloud layer whereas surface radiation will be influenced by all cloud layers present. It is possible that there are situations (e.g., deep convection) in which a cirrus anvil will be identified as a high cloud and optically thicker cloud-type groups below will have a more substantial influence on the surface radiation. The rapid decrease of radiation associated with the cumuliform cloud-type group can similarly be attributed to more optically thick and spatially robust cumuliform clouds during

afternoon deep convection. These results are also supportive of developing future pavement temperature forecasting not based solely on adjustments to surface radiation but considering a direct adjustment to pavement temperatures given cloud identification.

At sunset (00 UTC), the surface radiation distributions by cloud-type group exhibit a return to quasi-equilibrium conditions associated with the day night transition (Figure 4.15). The three hour differences in median radiation are not discussed below as the median values for radiation all approach approximately 100 Wm^{-2} for all cloud-type groups and 200 Wm^{-2} for clear conditions (Table 4.6). An important distinction to note between the sunset periods for surface radiation versus that of pavement temperature is that pavement temperatures did not approach quasi-equilibrium until some undetermined time after sunset (Figure 4.12, Table 4.5). As previously mentioned at the midday period, surface radiation is inherently better correlated with solar heating than the lag of pavement temperatures. This is also an important caution for future consideration of pavement temperatures after the day/night transition and accounting for the influence of longwave radiation.

Hourly surface radiation distribution observations allow for an increase in the temporal resolution to consider the differences among the surface radiation cloud-type groups (Figure 4.16 and Table 4.6). Again, the position of each cloud-type group is deliberate to suggest that there are similarities among clear, cumuliform cloud-type group and low cloud-type group. Clear conditions have the least within-group variation throughout the day (Figure 4.16) with a mean IQR of 89.2 Wm^{-2}. At 20 UTC there is an apparent outlier in the data set with a surface radiation observation close to 0 Wm^{-2} in the middle of the day. The outlier is excluded from statistical analyses. Cumuliform and high

cloud-type groups exhibit greater variability in the afternoon than in the morning (Figure 4.16). Cumuliform clouds have a mean morning (12 UTC though 17 UTC) IQR of 222.4 Wm^{-2} with an afternoon (19 UTC through 00 UTC) IQR of 311.5 Wm^{-2} (Table 4.6). Similarly high clouds have a mean morning IQR of 180.2 Wm^{-2} which increases during the afternoon to a mean IQR of 284.9 Wm^{-2} (Table 4.6). As previously discussed, the increase in afternoon variability with these two cloud-type groups is likely associated with limitations of the NRLCC algorithm for identifying multiple levels of cloud cover typically associates with afternoon deep convection. Low and middle cloud-type groups exhibit fairly large within group variation throughout the day (Figure 4.16). Low clouds have a mean IQR of 232.0 Wm^{-2} and middle clouds have a mean IQR of 185.6 Wm^{-2} for the entire day (Table 4.6). This large variability throughout the day suggests that the spatial coverage of such cloud cover is an important future consideration as well. Distinctions are not made among scattered low/middle cloud-type groups and more uniform low/middle cloud-type groups.

A unique comparison can be performed relating the mean observed surface radiation with the surface radiation computed in the SBDART sensitivity analysis. For all the cases, low clouds observed a mean surface radiation of 333.1 Wm^{-2} (Table 4.6) which is very similar to the SBDART low cloud mean total irradiance of 366.9 Wm^{-2} (Table 4.2). For all the cases, middle clouds observed a mean surface radiation of 239.1 Wm^{-2}. This value is much more closely associated with the total irradiance of thick middle/high clouds in the SBDART sensitivity analysis of approximately 240 Wm^{-2}. In the case study analysis, high clouds observe a mean radiation of 334.0 Wm^{-2} which lies between the values of the SBDART sensitivity analysis for thick middle/high clouds (240.5 Wm^{-2})

and low clouds (366.9 Wm^{-2}). This suggests that either the SBDART sensitivity analysis for thin middle/high clouds needs adjustment, or the more likely possibility that this provides another example of evidence suggesting the need for a ground-based cloud data set to compare with output from the NRLCC algorithm as it is unable to accurately access multi-level cloud scenarios. The high clouds throughout the case study analysis may be more associated with multiple levels of cloud cover and not simply a high cirrus canopy. The mean observed radiation for the cumuliform group in the case study analysis is 446.2 Wm^{-2}. The value lies between the SBDART sensitivity analysis values for low cloud (366.9 Wm^{-2}) and thin middle/high clouds (664.0 Wm^{-2}). It is important to note that a cumuliform cloud-type group was never exclusively modeled in the SBDART analysis. This comparison result suggests that, in the aggregate sense, while spatially robust and optically thick cumuliform associated with deep convection may rival the radiative influence of thick low clouds, spatially scattered cumuliform clouds will exhibit radiative influence more closely associated with optically thin high clouds. On a local scale, the temporal variation in passing scattered cloud cover over the RWIS sensor is the culprit.

The statistical analyses bring all three data sets together in an assessment of the relationships among pavement temperatures, surface radiation and cloud-type groups. Overall, for all the co-located sites throughout the two-week 1-16 June 2011 period, there is a direct relationship between surface radiation and pavement temperature (Figure 4.17). The correlation between surface radiation and pavement temperature is moderately strong with a correlation coefficient of 0.67 and statistically significant as well (Table 4.7). This result means that high radiation values are associated with higher pavement temperatures. This is to be expected as both variables are also diurnally dependent, and

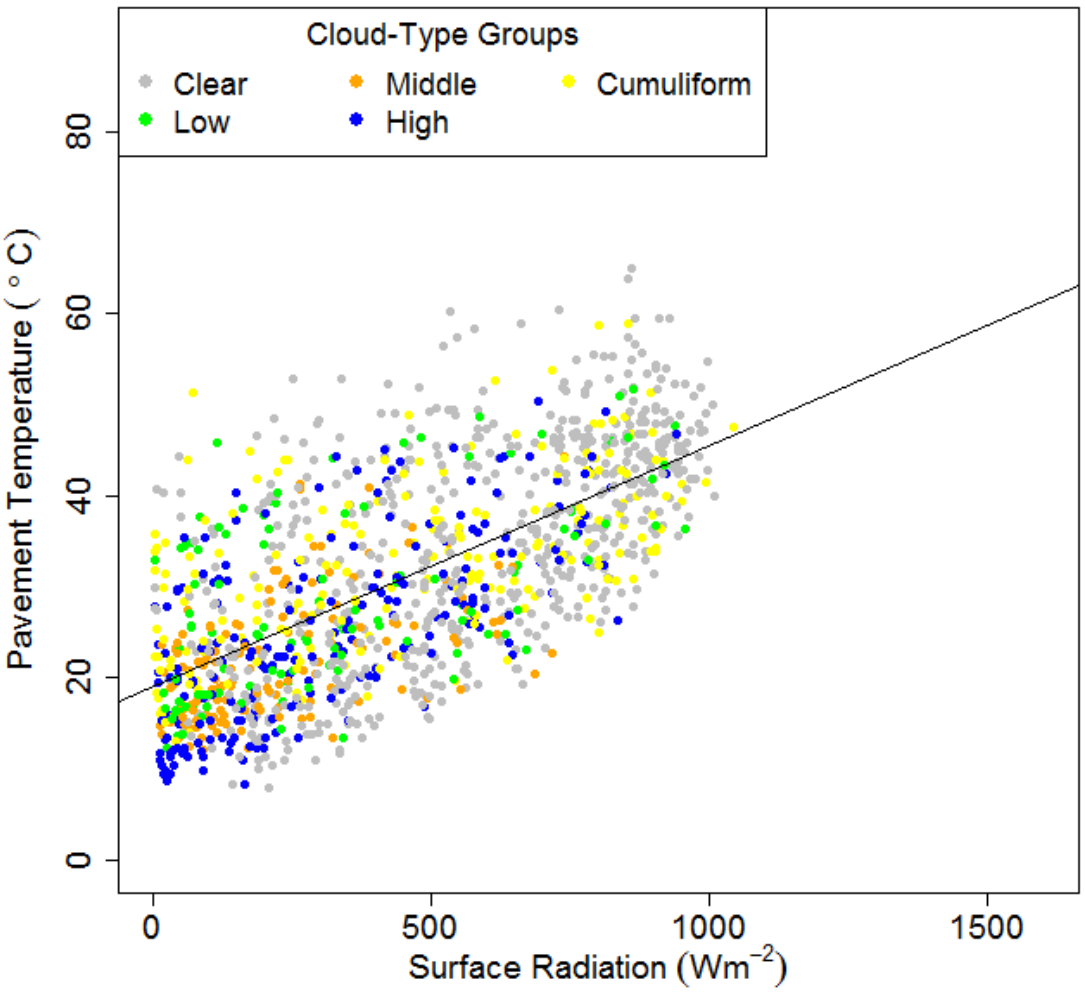

Figure 4.17. Overall scatterplot of surface radiation versus pavement temperature for all 13 co-located sites for the period 1-16 June 2011 colored by cloud-type group. The black line is the linear regression line.

Table 4.7. Surface radiation and pavement temperature TOD correlation analysis results for 1-16 June 2011 with Pearson's correlation coefficient (R), coefficient of determination (R^2), and p-value.

	12 UTC	**15 UTC**	**18 UTC**	**21 UTC**	**00 UTC**	**Overall**
R	-0.07	0.72	0.83	0.71	0.41	**0.67**
R^2	0.01	0.52	0.69	0.50	0.17	**0.45**
P-Value	0.48	< 0.01	< 0.01	< 0.01	< 0.01	**< 0.01**

TOD has yet to be considered. Further, this result indicates that approximately 45% of the variability in pavement temperature for this particular data set can be explained by the surface radiation.

In order to account for diurnal variability, the correlation analyses are also performed at the five primary TODs (Figures 4.18 and Table 4.7). Aside from sunrise, all correlation coefficients were significant. At sunrise, recall we observed our period of quasi-equilibrium. A tight cluster reveals not much variability among the variables (Figure 4.18). Two of the variables are weakly correlated at this period in which radiation versus pavement temperature has a non-significant correlation coefficient of -0.07 (Table 4.7). As the sun rises during the morning, there is more apparent separation among the variables with clear conditions shooting out ahead of cloudy conditions when considering the scatterplot (Figure 4.18). The correlation between surface radiation and pavement temperature is moderately strong during the morning TOD with a pavement temperature versus radiation coefficient of 0.72 (Table 4.7). At the midday TOD, the separation continues with clear conditions occupying the higher pavement temperatures and highest radiation observations. Cumuliform and high cloud-type groups are intermingled with some clear observations but are generally associated with slightly lower temperatures and radiation values. Low and middle cloud-type groups are associated with the lowest pavement temperature and surface radiation observations (Figure 4.18). At this TOD, the correlation between surface radiation and pavement temperature is strongest with a coefficient of 0.83 (Table 4.7). This result suggests that during the middle of the day during the peak solar heating, despite the lag in pavement temperature, higher temperature and higher radiation are associated. Further, in the middle of the day surface

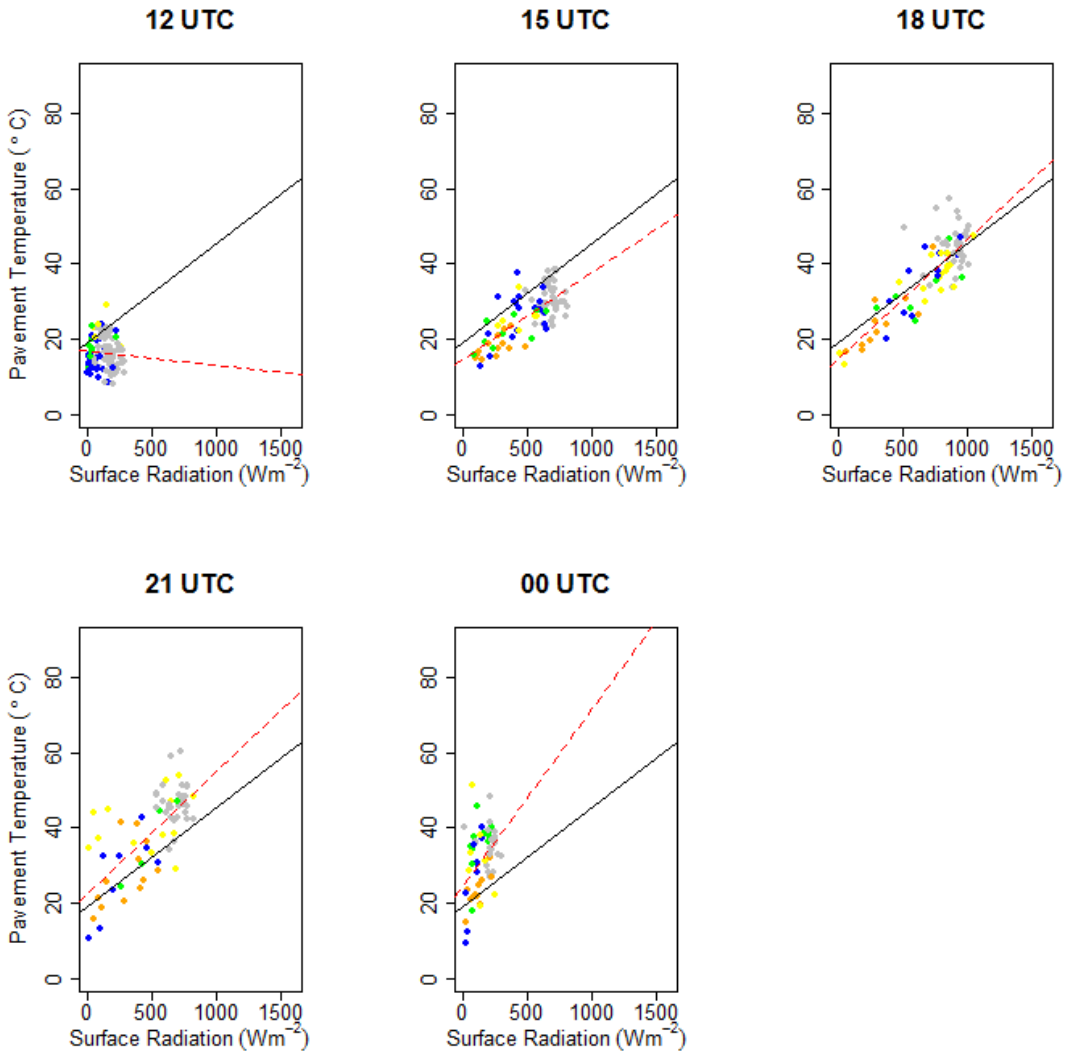

Figure 4.18. TOD scatterplots of surface radiation versus pavement temperature for all 13 co-located sites for the period 1-16 June 2011 colored by cloud-type groups; low (green), middle (orange), high (blue), cumuliform (yellow), and clear (gray). 12 UTC represents approximate sunrise, 15 UTC is a morning observation, 18 UTC represents the middle of the day in which typical peak solar heating occurs, 21 UTC is the afternoon and 00 UTC represents approximate sunset. The black line is the overall linear regression line shown in Figure 4.17. The dashed red line represents the linear regression line for each TOD.

radiation explains nearly 69% of the variability in pavement temperature. During the afternoon, the scatterplot of radiation versus pavement temperature appears to retreat and the divisions among cloud-type group begin to decay (Figure 4.18). Correlation between radiation and pavement temperature remains strong with a coefficient of 0.71 (Table 4.7). As was shown in the TOD and hourly distribution analyses, clear conditions warmed and cooled the fastest whereas cloud conditions lagged behind in their increases and decreases. The more vertical orientation of points (i.e., steeper slope) at sunset is related to the lag of pavement temperature with the loss of solar heating and the closer association between shortwave radiation and sunlight (Figure 4.18). Further, the correlation coefficient between surface radiation and pavement temperature decreases at sunset to 0.41 (Table 4.7).

Given that cloud-type groups are categorical data, a difference of medians statistical analysis for both pavement temperatures and surface radiation observations was performed at each TOD. All of the differences in medians observed at each TOD for both pavement temperature and surface radiation are significant (p-value < 0.01). This boosts confidence in the aforementioned comparisons and correlations from a statistical framework.

A linear regression analysis statistically confirms the relationships observed among pavement temperatures and surface radiation from 1-16 June 2011 for the 13 co-located sites (Figures 4.17 and 4.18, Table 4.8). It is important to remember that the regression parameters can only be considered valid for this particular data set. Overall, pavement temperatures vary by 0.026 °C/Wm^{-2} (Table 4.8). Recall that the SBDART sensitivity analysis and surface radiation distributions showed clouds affect radiation by

Table 4.8. TOD linear regression parameters from 1-16 June 2011 for surface radiation and pavement temperature.

Parameter	**12 UTC**	**15 UTC**	**18 UTC**	**21 UTC**	**00 UTC**	**Overall**
Intercept	16.780	14.799	14.890	22.616	24.790	**18.987**
Slope	-0.004	0.023	0.032	0.032	0.047	**0.026**

approximately 400 Wm^{-2}. These results combined suggest that clouds can impact pavement temperatures by approximately 10 °C. The pavement temperature distributions confirm that this is an appropriate range of influence. Near sunrise (12 UTC), the linear regression analysis confirms the quasi-equilibrium with an estimated slope parameter of -0.004 °C/Wm^{-2} (Table 4.8). There is little change among pavement temperature and surface radiation early in the day due to the fact that there is little direct sunlight at this TOD (Figure 4.18). Later in the morning at 15 UTC, the slope parameter increases to 0.023 °C/Wm^{-2}. Slope parameter estimates around midday (18 UTC) and afternoon (21 UTC) are identical at 0.032 °C/Wm^{-2} (Table 4.8). This result corresponds directly to the period of peak solar heating and typical peak surface temperatures as well. Towards sunset (00 UTC), the linear regression estimated slope parameter increases slightly to 0.047 °C/Wm^{-2} (Table 4.8). This increase in the slope is evidence of the lag associated with pavement temperatures and the reduction of direct sunlight (Figure 4.18). At sunset, surface radiation drops off considerably, though pavement temperatures lag behind due to the specific heat content of the material in question (i.e., asphalt versus concrete). These statistical results quantify the role of cloud cover in influencing pavement temperatures and surface radiation, and show the relationships among the variables as well.

d. Cross-Validation: Cloud Identified Versus Satellite Imagery

The final section of this analysis qualitatively assesses the accuracy of NRLCC algorithm output and the pixel matching methods by comparing the identified cloud-type group at each RWIS with visible satellite imagery. This cross-validation reveals that the NRLCC algorithm generally performs quite well despite complex cloud situations, though there are some apparent limitations with multi-level cloud scenarios. On the partly

cloudy 1 June 2011 case day, how well the NRLCC algorithm output transitions with different cloud-type groups is observed. In the morning (Figure 4.19), North Dakota is clear except for some high clouds identified in the southwestern corner of the state. Similarly, Iowa is mainly clear as well except for some high and middle clouds identified in the eastern part of the state. Kansas and Nebraska contain a far more complex cloud situation. A cirrus cloud deck is apparent in both visible imagery and algorithm output in eastern Nebraska. Lower clouds are identified southwest of this cirrus deck along the Kansas-Nebraska border. It is somewhat difficult to determine whether or not these low clouds are in fact more of a cumuliform, perhaps stratocumulus, cloud given the localized areal extent. Such NRLCC algorithm output confusion could explain similarities in the median time series among cumuliform and low cloud-type groups (Figure 4.14). Later around midday (Figure 4.20) while North Dakota and most of Iowa remain clear, the cirrus cloud deck progresses eastward into western parts of Iowa. The NRLCC algorithm output matches up well with this feature in the visibility satellite. The previously low clouds in Kansas now seem to be classified as cumuliform clouds. In the visible image it is apparent that some convective enhancement has occurred, though it is also possible that given the higher sun angle at midday rather than in the morning, the clouds will appear more reflective and thus brighter. This will lead to the NRLCC algorithm to detect higher pixel brightness values and classify a cumuliform rather than a low cloud. In the afternoon (Figure 4.21) the cirrus cloud deck has now propagated into central Iowa and is clearly visible in both satellite imagery and algorithm output. Additional convection has initiated near the Kansas-Nebraska border and all possible cloud-type groups are now identified throughout the region. This is suggestive of a multiple layer cloud situation in

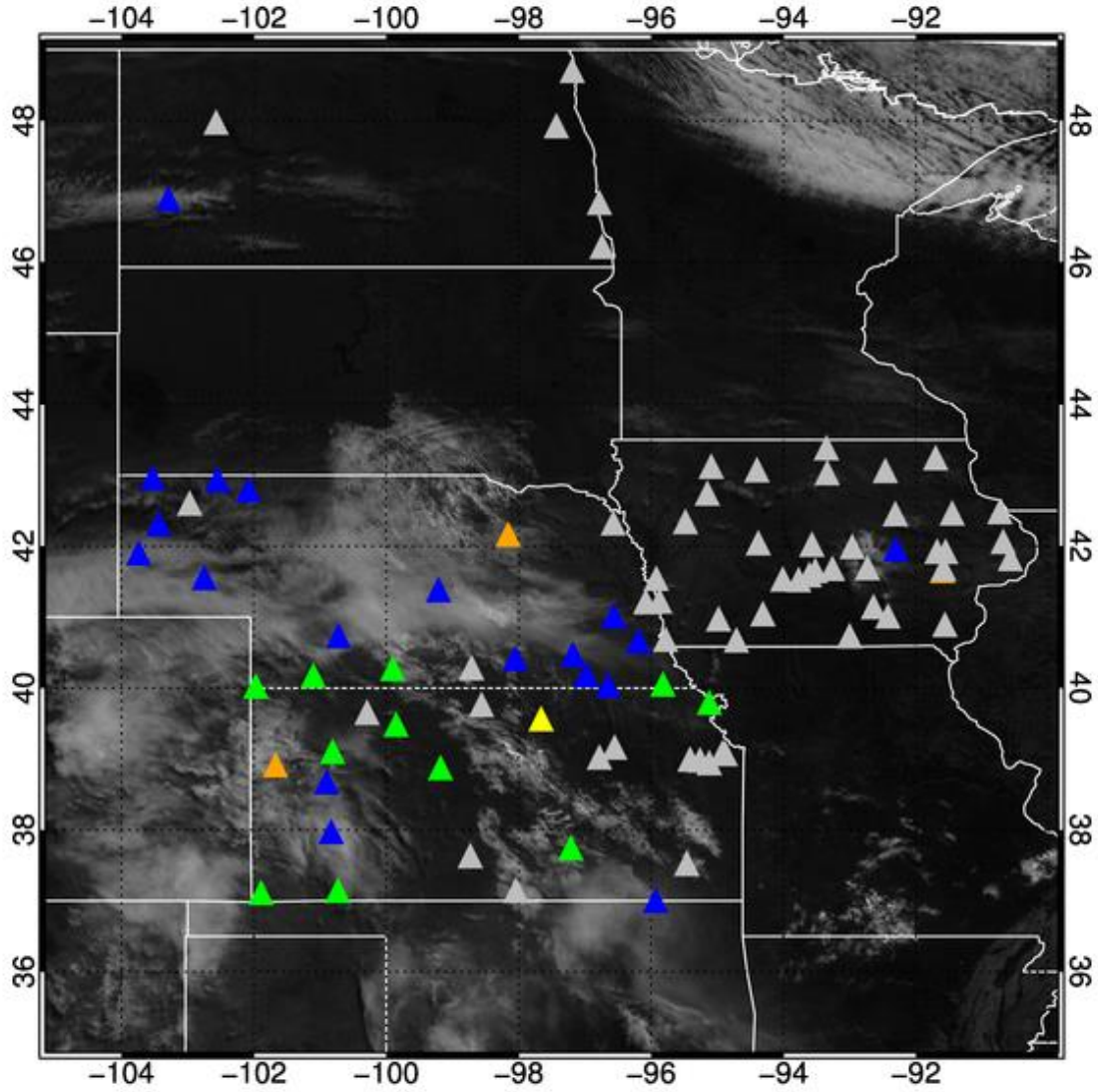

Figure 4.19. Partly cloudy, 15 UTC 1 June 2011 visible satellite imagery with NRLCC algorithm cloud-type group identified at RWIS sites overlaid.

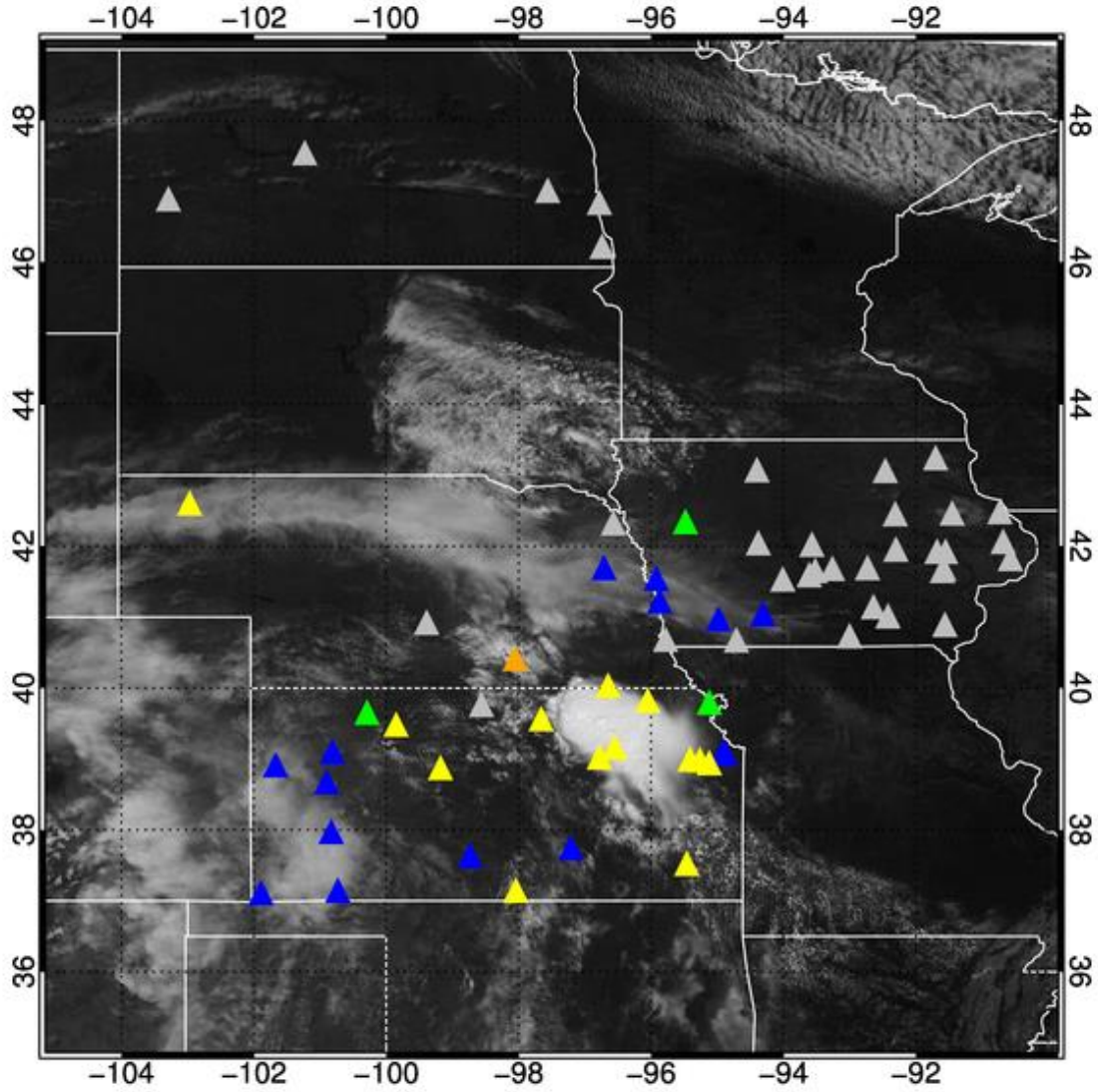

Figure 4.20. Partly cloudy, 18 UTC 1 June 2011 visible satellite imagery with NRLCC algorithm cloud-type group identified at RWIS sites overlaid.

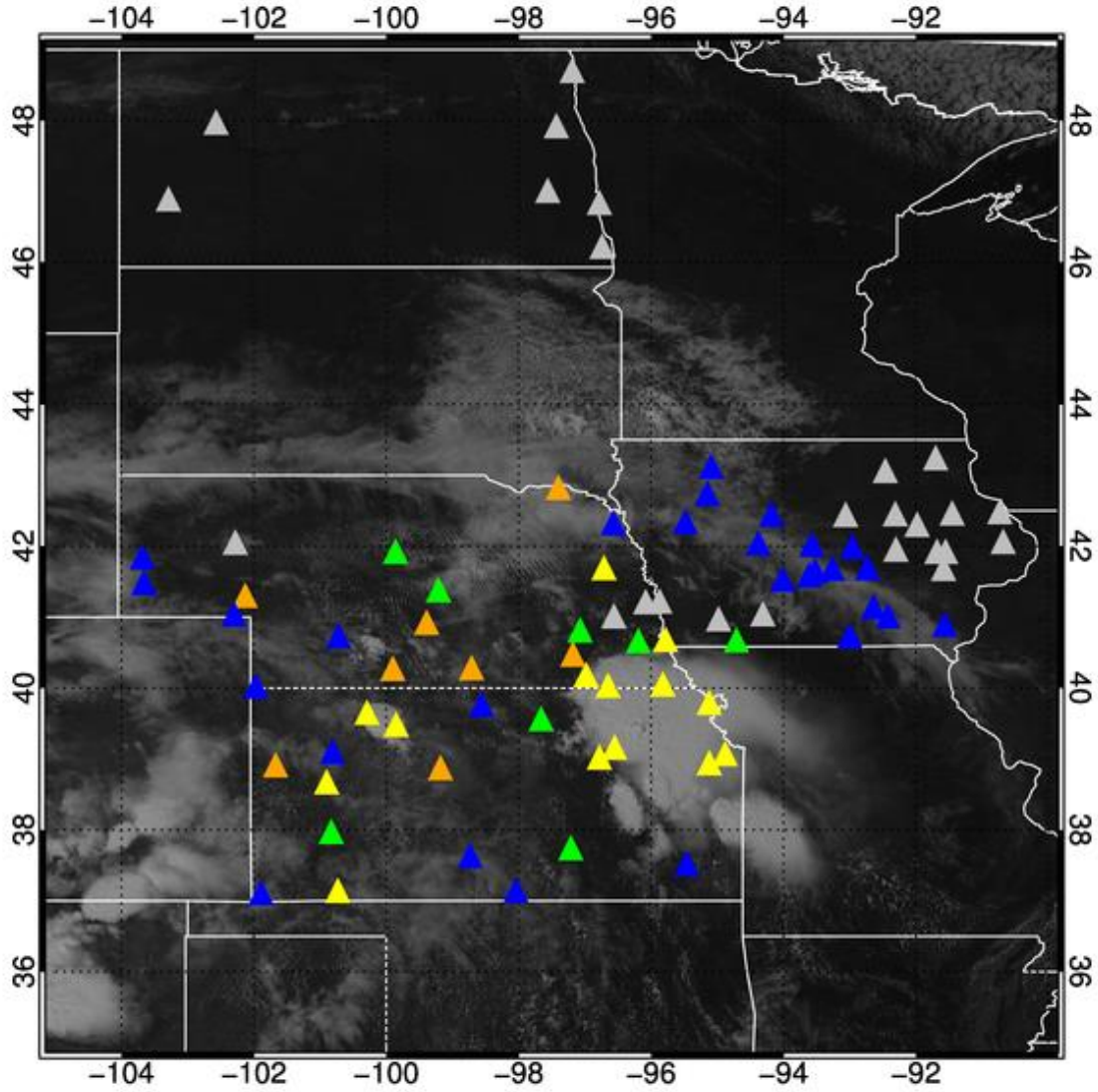

Figure 4.21. Partly cloudy, 21 UTC 1 June 2011 visible satellite imagery with NRLCC algorithm cloud-type group identified at RWIS sites overlaid.

which there is likely a high cloud canopy associated with the anvil of developing convection, while middle and low cloud-type groups are identified surrounding the convective complex.

An important test for the NRLCC algorithm output is to ensure that on a clear day (Figure 4.22) no clouds should be identified. Indeed, the algorithm and pixel matching perform quite well on this day. The algorithm and pixel matching are both sufficient to detect primarily clear conditions, and a localized area of low cloud cover in northern Kansas is easily identified by the algorithm. Such a result increases confidence in the algorithm being able to capture relatively localized cloud features and also supports the methods that allow for such localized cloud variability to be captured.

One final challenge for the NRLCC algorithm output is to consider how well it classifies cloud-type groups on a cloudy day (Figure 4.23). Kansas is the clearest of all states for this period. The low cloud identified in extreme northeastern Kansas could again be more of a stratocumulus, low cumuliform cloud based on the visible imagery. The cloud line in eastern Kansas does not appear due to a lack of RWIS sites (and primary roads) along such a corridor. In Nebraska, low clouds are generally identified in the western part of the state, middle in central Nebraska, and cumuliform clouds in the east. This result makes sense with a consideration of the synoptic conditions (Figure 3.10). This zonal classification of cloud-type groups is typical of what is associated with cold frontal passage. Cumuliform clouds will be associated with convection and transition to more of a stratiform shield associated with the relatively cooler, drier air mass in the post-frontal environment. A more mesoscale situation is apparent in the cloud-type groups identified in Iowa. Deep convection in the western part of the state is

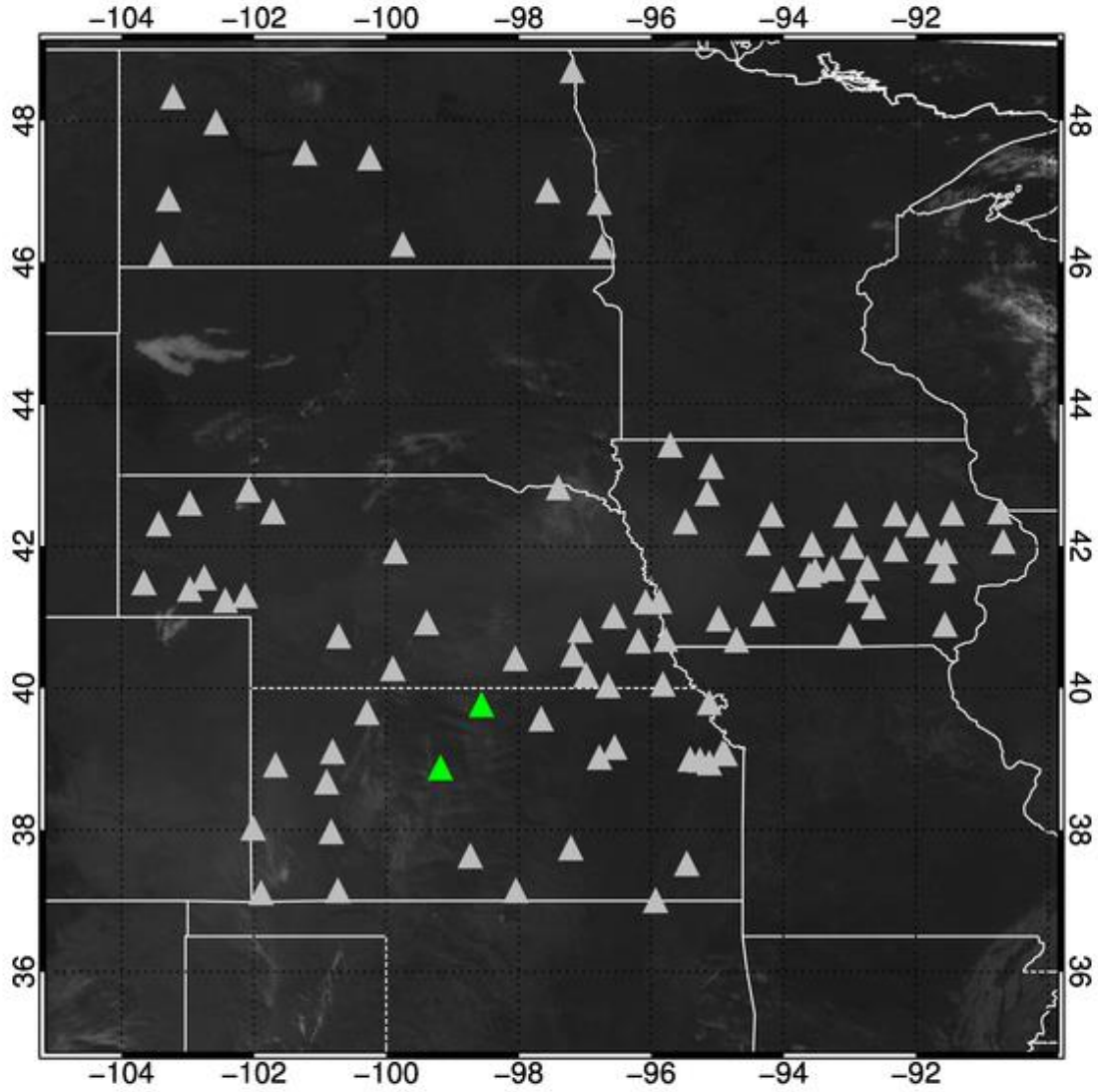

Figure 4.22. Clear day, 15 UTC 6 June 2011 visible satellite imagery with NRLCC algorithm cloud-type group identified at RWIS sites overlaid.

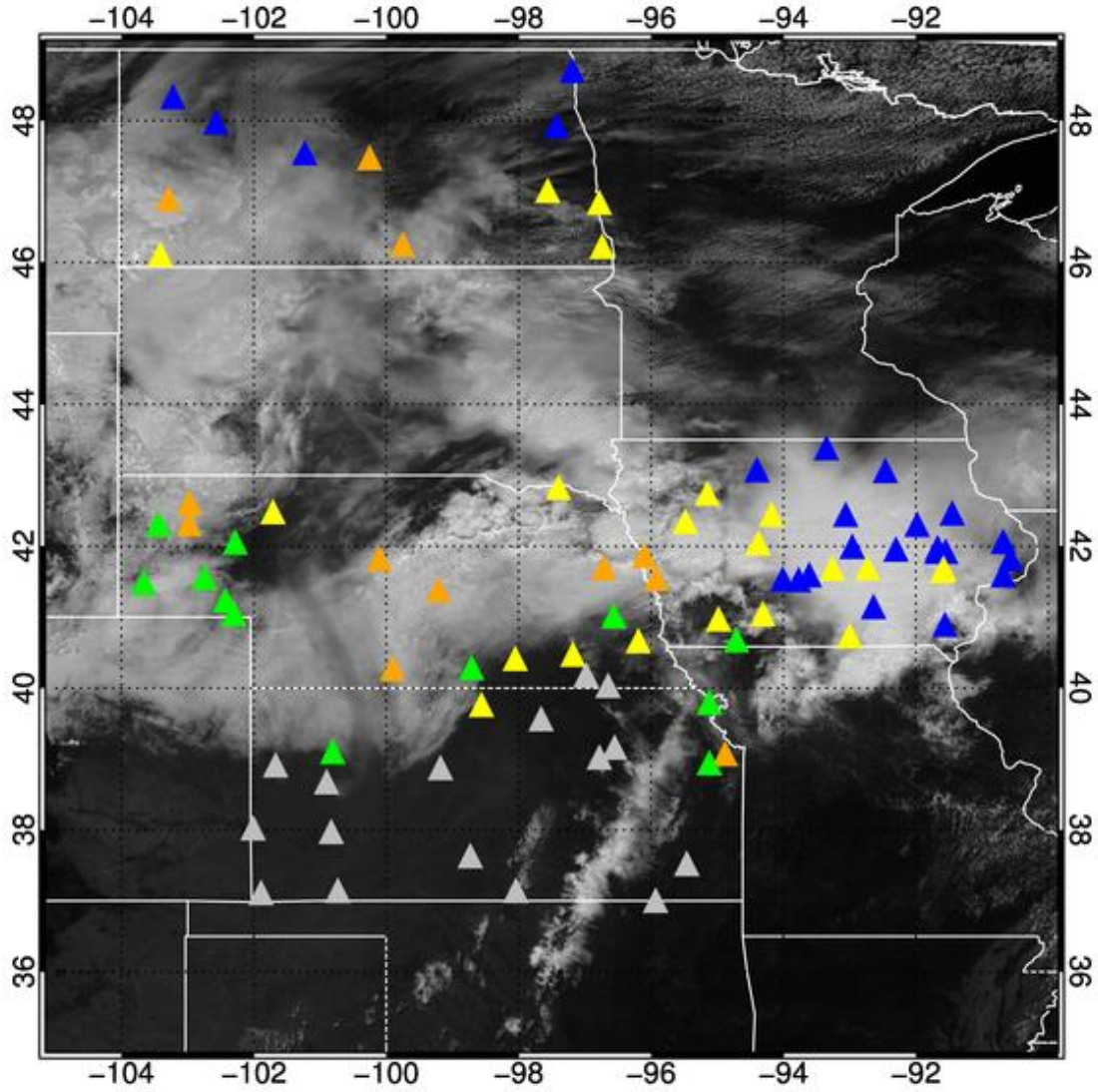

Figure 4.23. Cloudy day, 18 UTC 9 June 2011 visible satellite imagery with NRLCC algorithm cloud-type group identified at RWIS sites overlaid.

associated with cumuliform clouds whereas the cirrus anvil from this convection is identified as high clouds over eastern Iowa. It is important here to note that there are likely lower cloud layers beneath the cirrus anvil that are not able to be detected from the satellite-based NRLCC algorithm. North Dakota's cloud situation is once again suggestive of the synoptic situation with high clouds in the northern part of the state yielding to likely thicker, more spatially uniform and consistent middle and cumuliform cloud-type groups in the southern part of the state.

In this feasibility assessment, the NRLCC algorithm output and RWIS pixel matching method generally align quite well with visible satellite imagery for a variety of locations, areal extents and cloud situations. Some important caveats to note include the likelihood that high cloud-type group identification must be considered in context with the atmospheric situation. On the partly cloudy day (Figures 4.19-4.21) the high cloud (cirrus arc over Nebraska / Iowa) is less likely to be associated with cloud layers below (given the thin, wispy visible image appearance) than the high clouds on the cloudy day (Figure 4.23) associated with convection. Further, it is possible that, depending on sun angle and cloud height, some of the low clouds identified should be classified as cumuliform instead. Both of these factors combined likely explain why the median time series for the low, high and cumuliform cloud-type groups (Figure 4.14) are more closely related than the median time series of clear or middle clouds. The algorithm is superior at distinguishing cloud from clear, though there may be situations in which the specific subdivisions introduce error into the identification.

5. SUMMARY AND CONCLUSIONS

This assessment provides a first look at the application of remotely-sensed cloud information to determine the influence of cloud-type groups on pavement temperature and surface radiation and the correlations among pavement temperature, surface radiation and cloud-type groups. Results from an initial sensitivity study provide a framework for subsequent analyses. Results from a month-long and two-week period throughout the Great Plains quantify the magnitude of influence of cloud-type groups on pavement temperature variability. Statistical analyses extend such comparisons to include surface radiation as well. There is still uncertainty of how well the NRLCC algorithm can detect challenging (i.e., multiple level) cloud situations, though the algorithm generally performs well when considering identification output with visible satellite imagery.

The SBDART model allows for a simple radiative transfer sensitivity analysis in which the relative magnitude of influence of different cloud-type groups can be simulated. Further, brief consideration can be given to the role of water vapor in influencing radiative transfer as well. Overall, clouds provide substantial modification of the clear-sky radiative transfer. Although clouds were grouped into more general categories (i.e., low, middle, high), cloud optical thickness is identified as the most influential parameter when considering the radiative influence of clouds. Optically thick middle and high clouds had a simulated surface radiation of 240.5 Wm^{-2}. Low clouds of medium optical thickness had a simulated surface radiation of 366.9 Wm^{-2}. Optically thin middle and high level clouds had the least impact with surface radiation of 664.0 Wm^{-2}. Cloud variability can induce approximately 400 Wm^{-2} differences in surface radiation in the SBDART sensitivity analysis; however, the difference in surface radiation between

atmospheres with high and low water vapor concentrations is an order of magnitude smaller of approximately 25 Wm^{-2}. The simple sensitivity analysis results conform to previous literature on the influence of clouds on atmospheric radiative transfer.

This research fills a void in the literature by directly relating cloud cover to pavement temperatures. In a consideration of statistically significant differences among median pavement temperatures for the month of June 2011, clear conditions observe a median of 40.9 °C. The next highest observation is with cumuliform clouds at 34.9 °C. Low clouds lie in the middle of median temperatures at 31.5 °C. The second lowest cloud-type group is high clouds with a median of 27.9 °C and the coolest group is middle clouds at 23.7 °C. The results were similar for 1-16 June 2011 data as well. Considering observations at individual time stamps instead of throughout the entire data set removes diurnal dependence and allows for more meaningful comparisons. Clear conditions are clearly the highest pavement temperatures and have the smallest within-group variation throughout the day, but the largest diurnal variability. Low, high and cumuliform cloud-type groups exhibit tendencies in their pavement temperature median time series and distributions. This suggests that there is either some possible error in the NRLCC algorithm and/or optically thin high clouds will exhibit similar influence on pavement temperatures as spatially scattered (low and cumuliform) albeit optically thicker cloud-type groups. Middle clouds observed the most damped pavement temperature median time series which is expected given the likely spatially uniform and optically thicker nature of this cloud-type group.

Pavement temperature distribution analyses among cloud-type groups and surface radiation observations reveal similar tendencies as well. This is expected as pavement

temperature and surface radiation are moderately correlated (correlation coefficient of 0.67). This correlation increases to a coefficient of 0.83 when diurnal dependence is removed by considering specific TODs. Further, there is high confidence in the output from the NRLCC algorithm with the caveat that multi-level cloud situations and some low cumuliform clouds may have classification errors. Regardless, understanding these relationships is fundamental to the future goal of pavement temperature forecast improvement.

Ongoing research seeks to continue quantifying and considering different arrangements of cloud-type groups (e.g., spatial coverage in lieu of height groups) and the influence of such groups on pavement temperatures and surface radiation. Ultimately, the influence of cloud cover on nighttime pavement temperatures and longwave radiation must be a future avenue of research. These future studies will incorporate the same study region, though the temporal extent of the analyses will be broadened to include not only nighttime but different seasons of year as well. Understanding and quantifying these relationships is paramount to the development and feasibility assessments of assimilating cloud type output and modeling such sensitivity with the goal of increasing the accuracy of pavement temperature forecasts. In summary, the proposed future research includes conducting similar analyses for a broader time period to incorporate the effects of seasonality, assess alternative cloud information data sets (e.g., surface-based, CERES data), and perform model sensitivity assessments for pavement temperature forecasting.

REFERENCES

Ackerman, S. A., R. E. Holz, R. Frey, E. W. Eloranta, B. C. Maddux, and M. McGill, 2008: Cloud Detection with MODIS. Part II: Validation. *J. Atmos. Oceanic Technol.,* **25**, 1073–1086.

Bankert, R. L., 1994: Cloud Classification of AVHRR Imagery in Maritime Regions Using a Probabilistic Neural Network. *J. Appl. Meteor.*, **33**, 909–918.

Bankert, R. L., and R. H. Wade, 2007: Optimization of an Instance-Based GOES Cloud Classification Algorithm. *J. Appl. Meteor. Climatol.*, **46**, 36–49.

Bankert, R. L., C. Mitrescu, S. D. Miller, and R. H. Wade, 2009: Comparison of GOES Cloud Classification Algorithms Employing Explicit and Implicit Physics. *J. Appl. Meteor. Climatol.*, **48**, 1411–1421.

Bogren, J., 1991: Screening Effects on Road Surface Temperature and Road Slipperiness. *Theor. Appl. Climatol.*, **43**, 91–99.

Changnon, S. A., P. J. Lamb, and K. G. Hubbard, 1990: Regional Climate Centers: New Institutions for Climate Services and Climate-Impact Research. *Bull. Amer. Meteor. Soc.*, **71**, 527–537.

Chen, S.R., Cai, C.S., and B. Wolshon, 2009: From Normal Operation to Evacuation: Single-Vehicle Safety under Adverse Weather, Topographic and Operational Conditions. *Natural Hazards Review*, **10**, 68 – 76.

Chen, T., W. B. Rossow, and Y. Zhang, 2000: Radiative Effects of Cloud-Type Variations. *J. Climate*, **13**, 264–286.

Comprehensive Large Array-Data Stewardship System [CLASS], cited 2014: Environmental Data from Geostationary Satellites. Data retrieved on December 2, 2014 at http://www.nsof.class.noaa.gov/saa/products/search?datatype_family=GVAR_IMG.

Crevier, L., and Y. Delage, 2001: METRo: A New Model for Road-Condition Forecasting in Canada. *J. Appl. Meteor.*, **40**, 2026 – 2037.

Drobot, S., M. Chapman, C. Burghardt, S. Linden, and J. Cowie, 2012: The Toyota Racing Development Pavement Forecast Project. 90 pp. National Center for Atmospheric Research (NCAR), P.O. Box 3000, Boulder, Colorado, 80307.

Federal Highway Administration [FHWA], cited 2014: Road Weather Management Program. [Available online at http://ops.fhwa.dot.gov/weather/q1_roadimpact.htm.].

Google, cited 2014: Google Maps – Hubbard, Nebraska. Image retrieved on November 8, 2014 at https://www.google.com/maps/place/Hubbard,+NE+68741/@42.3858907,-96.5881141,1338m/data=!3m1!1e3!4m2!3m1!1s0x878e1d398372b235:0x85875907079ee13.

Hartmann, Dennis L., Maureen E. Ockert-Bell, Marc L. Michelsen, 1992: The Effect of Cloud Type on Earth's Energy Balance: Global Analysis. *J. Climate,* **5**, 1281 1304. doi:10.1175/1520-0442(1992)005<1281:TEOCTO>2.0.CO;2.

High Plains Regional Climate Center [HPRCC], cited 2013: Climate Data Services Classic Online Services. Data retrieved on June 1, 2013 at http://www.hprcc.unl.edu/services/index.php?p=online.

Khasawneh, M. A., and R. Y. Liang, 2012: Temperature Effect on Frictional Properties of HMA at Different Polishing Sites. *Jordan Journal of Civil Engineering*, **6**, 39 -53.

Liu, L., X. Sun, F. Chen, S. Zhao, and T. Gao, 2011: Cloud Classification Based on Structure Features of Infrared Images. *J. Atmos. Oceanic Technol.*, **28**, 410–417.

Meteorological Assimilation Data Ingest System [MADIS], cited 2014: MADIS. [Available online at http://madis.noaa.gov/.]

National Center for Atmospheric Research [NCAR] , cited 2014a: Maintenance Decision Support System. [Available online at http://ral.ucar.edu/projects/rdwx_mdss/.]

NCAR, cited 2014b: A comparison of road temperature models: FASST, METRo, and SNTHERM. Version 2.0. [Available online at www.rap.ucar.edu/projects/rdwx_mdss/documents/RoadModel_ Comparison_Report_ v2.0_8_3_07.pdf.]

NCAR, cited 2014c: High Performance Storage System. [Available online at https://www2.cisl.ucar.edu/docs/hpss.]

National Oceanic and Atmospheric Administration [NOAA], cited 2014: Weather-Ready Nation. [Available online at http://www.nws.noaa.gov/com/weatherreadynation/#.VGh20MnZcYI.]

Naval Research Laboratory [NRL], cited 2013: NRL Monterey GOES Cloud Classification. [Available online at http://www.nrlmry.navy.mil/sat bin/clouds.cgi.]

Pisano, P.A., Goodwin, L.C., and M.A. Rosetti, 2008: U.S. Highway Crashes In Adverse Road Weather Conditions. *Proceedings of the 88th Annual American Meteorological Society Meeting*, 20-24 January, New Orleans, LA.

Ricchiazzi, Paul, Shiren Yang, Catherine Gautier, David Sowle, 1998: SBDART: A Research and Teaching Software Tool for Plane-Parallel Radiative Transfer in the Earth's Atmosphere. *Bull. Amer. Meteor. Soc.*, **79**, 2101–2114.

Rutz, J. J., and C. V. Gibson, 2013: Integration of a Road Surface Model into NWS Operations. *Bull. Amer. Meteor. Soc.*, **94**, 1495–1500.

SBDART. 2013. *SBDART: A Practical Tool for Plane-Parallel Radiative Transfer in Earth's Atmosphere.* Accessed on November 11, 2013 at http://arm.mrcsb.com/sbdart/html/sbdart-intro.html.

Stephens, G. L., and S. C. Tsay, 1990: On the cloud absorption anomaly. *Q. J. R. Meteorol. SOC.*, **116**, 671–704.

Stephens, G. L., 2005: Cloud Feedbacks in the Climate System: A Critical Review. *J. Climate*, **18**, 237–273.

Tag, P. M., R. L. Bankert, and L. R. Brody, 2000: An AVHRR Multiple Cloud-Type Classification Package. *J. Appl. Meteor.*, **39**, 125–134.

Vaisala, cited 2014: Road Solutions – Road Weather Sensors. [Available online at http://www.vaisala.com/en/roads/products/roadweathersensors/Pages/default.aspx.]

Várnai, T., and R. Davies, 1999: Effects of Cloud Heterogeneities on Shortwave Radiation: Comparison of Cloud-Top Variability and Internal Heterogeneity. *J. Atmos. Sci.*, **56**, 4206–4224.

Weather Prediction Center [WPC], cited 2014: WPC Surface Analysis Archive. Images retrieved on November 8, 2014 at http://www.wpc.ncep.noaa.gov/archives/web_pages/sfc/sfc_archive.php.

Wielicki, B. A., B. R. Barkstrom, E. F. Harrison, R. B. Lee, G. L. Smith, and J. E. Cooper, 1996: Clouds and the Earth's Radiant Energy System (CERES): An Earth Observing System Experiment. *Bull. Amer. Meteor. Soc.*, **77**, 853–868.

Yang, J., W. Lu, Y. Ma, W. Yao, 2012: An Automated Cirrus Cloud Detection Method for a Ground-Based Cloud Image. *J. Atmos. Oceanic Technol.*, **29**, 527–537.